Measurement of the inclusive electron spectrum from B meson decays and determination of $|V_{ub}|$

J. P. Lees,[1] V. Poireau,[1] V. Tisserand,[1] E. Grauges,[2] A. Palano,[3] G. Eigen,[4] D. N. Brown,[5] Yu. G. Kolomensky,[5] H. Koch,[6] T. Schroeder,[6] C. Hearty,[7] T. S. Mattison,[7] J. A. McKenna,[7] R. Y. So,[7] V. E. Blinov,[8a,8b,8c] A. R. Buzykaev,[8a] V. P. Druzhinin,[8a,8b] V. B. Golubev,[8a,8b] E. A. Kravchenko,[8a,8b] A. P. Onuchin,[8a,8b,8c] S. I. Serednyakov,[8a,8b] Yu. I. Skovpen,[8a,8b] E. P. Solodov,[8a,8b] K. Yu. Todyshev,[8a,8b] A. J. Lankford,[9] J. W. Gary,[10] O. Long,[10] A. M. Eisner,[11] W. S. Lockman,[11] W. Panduro Vazquez,[11] D. S. Chao,[12] C. H. Cheng,[12] B. Echenard,[12] K. T. Flood,[12] D. G. Hitlin,[12] J. Kim,[12] T. S. Miyashita,[12] P. Ongmongkolkul,[12] F. C. Porter,[12] M. Röhrken,[12] Z. Huard,[13] B. T. Meadows,[13] B. G. Pushpawela,[13] M. D. Sokoloff,[13] L. Sun,[13,†] J. G. Smith,[14] S. R. Wagner,[14] D. Bernard,[15] M. Verderi,[15] D. Bettoni,[16a] C. Bozzi,[16a] R. Calabrese,[16a,16b] G. Cibinetto,[16a,16b] E. Fioravanti,[16a,16b] I. Garzia,[16a,16b] E. Luppi,[16a,16b] V. Santoro,[16a] A. Calcaterra,[17] R. de Sangro,[17] G. Finocchiaro,[17] S. Martellotti,[17] P. Patteri,[17] I. M. Peruzzi,[17] M. Piccolo,[17] M. Rotondo,[17] A. Zallo,[17] S. Passaggio,[18] C. Patrignani,[18,‡] B. Bhuyan,[19] U. Mallik,[20] C. Chen,[21] J. Cochran,[21] S. Prell,[21] H. Ahmed,[22] A. V. Gritsan,[23] N. Arnaud,[24] M. Davier,[24] F. Le Diberder,[24] A. M. Lutz,[24] G. Wormser,[24] D. J. Lange,[25] D. M. Wright,[25] J. P. Coleman,[26] E. Gabathuler,[26] D. E. Hutchcroft,[26] D. J. Payne,[26] C. Touramanis,[26] A. J. Bevan,[27] F. Di Lodovico,[27] R. Sacco,[27] G. Cowan,[28] Sw. Banerjee,[29] D. N. Brown,[29] C. L. Davis,[29] A. G. Denig,[30] M. Fritsch,[30] W. Gradl,[30] K. Griessinger,[30] A. Hafner,[30] K. R. Schubert,[30] R. J. Barlow,[31,§] G. D. Lafferty,[31] R. Cenci,[32] A. Jawahery,[32] D. A. Roberts,[32] R. Cowan,[33] R. Cheaib,[34] S. H. Robertson,[34] B. Dey,[35a] N. Neri,[35a] F. Palombo,[35a,35b] L. Cremaldi,[36] R. Godang,[36,¶] D. J. Summers,[36] P. Taras,[37] G. De Nardo,[38] C. Sciacca,[38] G. Raven,[39] C. P. Jessop,[40] J. M. LoSecco,[40] K. Honscheid,[41] R. Kass,[41] A. Gaz,[42a] M. Margoni,[42a,42b] M. Posocco,[42a] G. Simi,[42a,42b] F. Simonetto,[42a,42b] R. Stroili,[42a,42b] S. Akar,[43] E. Ben-Haim,[43] M. Bomben,[43] G. R. Bonneaud,[43] G. Calderini,[43] J. Chauveau,[43] G. Marchiori,[43] J. Ocariz,[43] M. Biasini,[44a,44b] E. Manoni,[44a] A. Rossi,[44a] G. Batignani,[45a,45b] S. Bettarini,[45a,45b] M. Carpinelli,[45a,45b,**] G. Casarosa,[45a,45b] M. Chrzaszcz,[45a] F. Forti,[45a,45b] M. A. Giorgi,[45a,45b] A. Lusiani,[45a,45c] B. Oberhof,[45a,45b] E. Paoloni,[45a,45b] M. Rama,[45a] G. Rizzo,[45a,45b] J. J. Walsh,[45a] A. J. S. Smith,[46] F. Anulli,[47a] R. Faccini,[47a,47b] F. Ferrarotto,[47a] F. Ferroni,[47a,47b] A. Pilloni,[47a,47b] G. Piredda,[47a,*] C. Bünger,[48] S. Dittrich,[48] O. Grünberg,[48] M. Heß,[48] T. Leddig,[48] C. Voß,[48] R. Waldi,[48] T. Adye,[49] F. F. Wilson,[49] S. Emery,[50] G. Vasseur,[50] D. Aston,[51] C. Cartaro,[51] M. R. Convery,[51] J. Dorfan,[51] W. Dunwoodie,[51] M. Ebert,[51] R. C. Field,[51] B. G. Fulsom,[51] M. T. Graham,[51] C. Hast,[51] W. R. Innes,[51] P. Kim,[51] D. W. G. S. Leith,[51] S. Luitz,[51] V. Luth,[51] D. B. MacFarlane,[51] D. R. Muller,[51] H. Neal,[51] B. N. Ratcliff,[51] A. Roodman,[51] M. K. Sullivan,[51] J. Va'vra,[51] W. J. Wisniewski,[51] M. V. Purohit,[52] J. R. Wilson,[52] A. Randle-Conde,[53] S. J. Sekula,[53] M. Bellis,[54] P. R. Burchat,[54] E. M. T. Puccio,[54] M. S. Alam,[55] J. A. Ernst,[55] R. Gorodeisky,[56] N. Guttman,[56] D. R. Peimer,[56] A. Soffer,[56] S. M. Spanier,[57] J. L. Ritchie,[58] R. F. Schwitters,[58] J. M. Izen,[59] X. C. Lou,[59] F. Bianchi,[60a,60b] F. De Mori,[60a,60b] A. Filippi,[60a] D. Gamba,[60a,60b] L. Lanceri,[61] L. Vitale,[61] F. Martinez-Vidal,[62] A. Oyanguren,[62] J. Albert,[63] A. Beaulieu,[63] F. U. Bernlochner,[63] G. J. King,[63] R. Kowalewski,[63] T. Lueck,[63] I. M. Nugent,[63] J. M. Roney,[63] N. Tasneem,[63] T. J. Gershon,[64] P. F. Harrison,[64] T. E. Latham,[64] R. Prepost,[65] and S. L. Wu[65]

(*BABAR* Collaboration)

[1]*Laboratoire d'Annecy-le-Vieux de Physique des Particules (LAPP), Université de Savoie, CNRS/IN2P3, F-74941 Annecy-Le-Vieux, France*
[2]*Universitat de Barcelona, Facultat de Fisica, Departament ECM, E-08028 Barcelona, Spain*
[3]*INFN Sezione di Bari and Dipartimento di Fisica, Università di Bari, I-70126 Bari, Italy*
[4]*University of Bergen, Institute of Physics, N-5007 Bergen, Norway*
[5]*Lawrence Berkeley National Laboratory and University of California, Berkeley, California 94720, USA*
[6]*Ruhr Universität Bochum, Institut für Experimentalphysik 1, D-44780 Bochum, Germany*
[7]*University of British Columbia, Vancouver, British Columbia, Canada V6T 1Z1*
[8a]*Budker Institute of Nuclear Physics SB RAS, Novosibirsk 630090, Russia*
[8b]*Novosibirsk State University, Novosibirsk 630090, Russia*
[8c]*Novosibirsk State Technical University, Novosibirsk 630092, Russia*
[9]*University of California at Irvine, Irvine, California 92697, USA*
[10]*University of California at Riverside, Riverside, California 92521, USA*
[11]*University of California at Santa Cruz, Institute for Particle Physics, Santa Cruz, California 95064, USA*
[12]*California Institute of Technology, Pasadena, California 91125, USA*
[13]*University of Cincinnati, Cincinnati, Ohio 45221, USA*
[14]*University of Colorado, Boulder, Colorado 80309, USA*
[15]*Laboratoire Leprince-Ringuet, Ecole Polytechnique, CNRS/IN2P3, F-91128 Palaiseau, France*
[16a]*INFN Sezione di Ferrara, I-44122 Ferrara, Italy*
[16b]*Dipartimento di Fisica e Scienze della Terra, Università di Ferrara, I-44122 Ferrara, Italy*

[17]*INFN Laboratori Nazionali di Frascati, I-00044 Frascati, Italy*

[18]*INFN Sezione di Genova, I-16146 Genova, Italy*

[19]*Indian Institute of Technology Guwahati, Guwahati, Assam 781 039, India*

[20]*University of Iowa, Iowa City, Iowa 52242, USA*

[21]*Iowa State University, Ames, Iowa 50011, USA*

[22]*Physics Department, Jazan University, Jazan 22822, Kingdom of Saudi Arabia*

[23]*Johns Hopkins University, Baltimore, Maryland 21218, USA*

[24]*Laboratoire de l'Accélérateur Linéaire, IN2P3/CNRS et Université Paris-Sud 11, Centre Scientifique d'Orsay, F-91898 Orsay Cedex, France*

[25]*Lawrence Livermore National Laboratory, Livermore, California 94550, USA*

[26]*University of Liverpool, Liverpool L69 7ZE, United Kingdom*

[27]*Queen Mary, University of London, London, E1 4NS, United Kingdom*

[28]*University of London, Royal Holloway and Bedford New College, Egham, Surrey TW20 0EX, United Kingdom*

[29]*University of Louisville, Louisville, Kentucky 40292, USA*

[30]*Johannes Gutenberg-Universität Mainz, Institut für Kernphysik, D-55099 Mainz, Germany*

[31]*University of Manchester, Manchester M13 9PL, United Kingdom*

[32]*University of Maryland, College Park, Maryland 20742, USA*

[33]*Massachusetts Institute of Technology, Laboratory for Nuclear Science, Cambridge, Massachusetts 02139, USA*

[34]*McGill University, Montréal, Québec, Canada H3A 2T8*

[35a]*INFN Sezione di Milano, I-20133 Milano, Italy*

[35b]*Dipartimento di Fisica, Università di Milano, I-20133 Milano, Italy*

[36]*University of Mississippi, University, Mississippi 38677, USA*

[37]*Université de Montréal, Physique des Particules, Montréal, Québec, Canada H3C 3J7*

[38]*INFN Sezione di Napoli and Dipartimento di Scienze Fisiche, Università di Napoli Federico II, I-80126 Napoli, Italy*

[39]*NIKHEF, National Institute for Nuclear Physics and High Energy Physics, NL-1009 DB Amsterdam, The Netherlands*

[40]*University of Notre Dame, Notre Dame, Indiana 46556, USA*

[41]*Ohio State University, Columbus, Ohio 43210, USA*

[42a]*INFN Sezione di Padova, I-35131 Padova, Italy*

[42b]*Dipartimento di Fisica, Università di Padova, I-35131 Padova, Italy*

[43]*Laboratoire de Physique Nucléaire et de Hautes Energies, IN2P3/CNRS, Université Pierre et Marie Curie-Paris6, Université Denis Diderot-Paris7, F-75252 Paris, France*

[44a]*INFN Sezione di Perugia, I-06123 Perugia, Italy*

[44b]*Dipartimento di Fisica, Università di Perugia, I-06123 Perugia, Italy*

[45a]*INFN Sezione di Pisa, I-56127 Pisa, Italy*

[45b]*Dipartimento di Fisica, Università di Pisa, I-56127 Pisa, Italy*

[45c]*Scuola Normale Superiore di Pisa, I-56127 Pisa, Italy*

[46]*Princeton University, Princeton, New Jersey 08544, USA*

[47a]*INFN Sezione di Roma, I-00185 Roma, Italy*

[47b]*Dipartimento di Fisica, Università di Roma La Sapienza, I-00185 Roma, Italy*

[48]*Universität Rostock, D-18051 Rostock, Germany*

[49]*Rutherford Appleton Laboratory, Chilton, Didcot, Oxon, OX11 0QX, United Kingdom*

[50]*CEA, Irfu, SPP, Centre de Saclay, F-91191 Gif-sur-Yvette, France*

[51]*SLAC National Accelerator Laboratory, Stanford, California 94309 USA*

[52]*University of South Carolina, Columbia, South Carolina 29208, USA*

[53]*Southern Methodist University, Dallas, Texas 75275, USA*

[54]*Stanford University, Stanford, California 94305, USA*

[55]*State University of New York, Albany, New York 12222, USA*

[56]*Tel Aviv University, School of Physics and Astronomy, Tel Aviv, 69978, Israel*

[57]*University of Tennessee, Knoxville, Tennessee 37996, USA*

[58]*University of Texas at Austin, Austin, Texas 78712, USA*

[59]*University of Texas at Dallas, Richardson, Texas 75083, USA*

[60a]*INFN Sezione di Torino, I-10125 Torino, Italy*

[60b]*Dipartimento di Fisica, Università di Torino, I-10125 Torino, Italy*

[61]*INFN Sezione di Trieste and Dipartimento di Fisica, Università di Trieste, I-34127 Trieste, Italy*

[62]*IFIC, Universitat de Valencia-CSIC, E-46071 Valencia, Spain*

^{63}University of Victoria, Victoria, British Columbia, Canada V8W 3P6
^{64}Department of Physics, University of Warwick, Coventry CV4 7AL, United Kingdom
^{65}University of Wisconsin, Madison, Wisconsin 53706, USA

Based on the full *BABAR* data sample of 466.5 million $B\bar{B}$ pairs, we present measurements of the electron spectrum from semileptonic B meson decays. We fit the inclusive electron spectrum to distinguish Cabibbo-Kobayashi-Maskawa (CKM) suppressed $B \to X_u e\nu$ decays from the CKM-favored $B \to X_c e\nu$ decays, and from various other backgrounds, and determine the total semileptonic branching fraction $\mathcal{B}(B \to Xe\nu) = (10.34 \pm 0.04_{\text{stat}} \pm 0.26_{\text{syst}})\%$, averaged over $B^{\pm}$ and B^0 mesons. We determine the spectrum and branching fraction for charmless $B \to X_u e\nu$ decays and extract the CKM element $|V_{ub}|$, by relying on four different QCD calculations based on the heavy quark expansion. While experimentally, the electron momentum region above 2.1 GeV/c is favored, because the background is relatively low, the uncertainties for the theoretical predictions are largest in the region near the kinematic endpoint. Detailed studies to assess the impact of these four predictions on the measurements of the electron spectrum, the branching fraction, and the extraction of the CKM matrix element $|V_{ub}|$ are presented, with the lower limit on the electron momentum varied from 0.8 GeV/c to the kinematic endpoint. We determine $|V_{ub}|$ using each of these different calculations and find, $|V_{ub}| = (3.794 \pm 0.107_{\text{exp}}\,^{+0.292}_{-0.219\,\text{SF}}\,^{+0.078}_{-0.068\,\text{theory}}) \times 10^{-3}$ (De Fazio and Neubert), $(4.563 \pm 0.126_{\text{exp}}\,^{+0.230}_{-0.208\,\text{SF}}\,^{+0.162}_{-0.163\,\text{theory}}) \times 10^{-3}$ (Bosch, Lange, Neubert, and Paz), $(3.959 \pm 0.104_{\text{exp}}\,^{+0.164}_{-0.154\,\text{SF}}\,^{+0.042}_{-0.079\,\text{theory}}) \times 10^{-3}$ (Gambino, Giordano, Ossola, and Uraltsev), $(3.848 \pm 0.108_{\text{exp}}\,^{+0.084}_{-0.070\,\text{theory}}) \times 10^{-3}$ (dressed gluon exponentiation), where the stated uncertainties refer to the experimental uncertainties of the partial branching fraction measurement, the shape function parameters, and the theoretical calculations.

I. INTRODUCTION

Semileptonic decays of B mesons proceed via leading order weak interactions. They are expected to be free of non-Standard-Model contributions and therefore play a critical role in the determination of the Cabibbo-Kobayashi-Maskawa (CKM) quark-mixing matrix [1] elements $|V_{cb}|$ and $|V_{ub}|$. In the Standard Model (SM), the CKM elements satisfy unitarity relations that can be illustrated geometrically as triangles in the complex plane. For one of these triangles, CP asymmetries determine the angles, $|V_{cb}|$ normalizes the length of the sides, and the ratio $|V_{ub}|/|V_{cb}|$ determines the side opposite the well-measured angle β. Thus, precise measurements of $|V_{cb}|$ and $|V_{ub}|$ are crucial to studies of flavor physics and CP violation in the quark sector.

There are two methods to determine $|V_{cb}|$ and $|V_{ub}|$, one based on exclusive semileptonic B decays, where the hadron in the final state is a D, D^*, D^{**} or $\pi, \rho, \omega, \eta, \eta'$ meson, the other based on inclusive decays $B \to Xe\nu$,

where X refers to either X_c or X_u, i.e., to any hadronic state with or without charm, respectively.

The extractions of $|V_{cb}|$ and $|V_{ub}|$ from measured inclusive or exclusive semileptonic B meson decays rely on different experimental techniques to isolate the signal and on different theoretical descriptions of QCD contributions to the underlying weak decay processes. Thus, they have largely independent uncertainties, and provide important cross-checks of the methods and our understanding of these decays in general. At present, these two methods result in values for $|V_{cb}|$ and $|V_{ub}|$ that each differ by approximately 3 standard deviations [2].

In this paper, we present a measurement of the inclusive electron momentum spectrum and branching fraction (BF) for the sum of all semileptonic $B \to Xe\nu$ decays, as well as measurements of the spectrum and partial BF for charmless semileptonic $B \to X_u e\nu$ decays. The total rate for the $B \to X_u e\nu$ decays is suppressed by about a factor 50 compared to the $B \to X_c e\nu$ decays. This background dominates the signal spectrum except near the high-momentum endpoint. In the rest frame of the B meson, the electron spectrum for $B \to X_u e\nu$ signal extends to $\sim$2.6 GeV/c, while for the background $B \to X_c e\nu$ decays the kinematic endpoint is at $\sim$2.3 GeV/c. In the $\Upsilon(4S)$ rest frame, the two B mesons are produced with momenta of 300 MeV/c which extends the electron endpoint by about 200 MeV/c. The endpoint region above 2.3 GeV/c, which covers only about 10% of the total electron spectrum, is more suited for the experimental isolation of the charmless decays.

*Deceased
†Present address: Wuhan University, Wuhan 43072, China.
‡Present address: Università di Bologna and INFN Sezione di Bologna, I-47921 Rimini, Italy.
§Present address: University of Huddersfield, Huddersfield HD1 3DH, United Kingdom.
¶Present address: University of South Alabama, Mobile, Alabama 36688, USA.
**Present address: Università di Sassari, I-07100 Sassari, Italy.

To distinguish contributions of the CKM suppressed $B \rightarrow X_u e\nu$ decays from those of CKM-favored $B \rightarrow X_c e\nu$ decays, and from various other backgrounds, we fit the inclusive electron momentum spectrum, averaged over $B^\pm$ and B^0 mesons produced in the $\Upsilon(4S)$ decays [2,3]. For this fit, we need predictions for the shape of the $B \rightarrow X_u e\nu$ spectrum. We have employed and studied four different QCD calculations based on the heavy quark expansion (HQE) [4]. The upper limit of the fitted range of the momentum spectrum is fixed at 3.5 GeV/c, while the lower limit extends down to 0.8 GeV/c, covering up to 90% of the total signal electron spectrum. From the fitted spectrum we derive the partial BF for charmless $B \rightarrow X_u e\nu$ decays and extract the CKM element $|V_{ub}|$. While the experimental sensitivity to the $B \rightarrow X_u e\nu$ spectrum and to $|V_{ub}|$ is primarily determined from the spectrum above 2.1 GeV/c, due to very large backgrounds at lower momenta, the uncertainties for the theoretical predictions are largest in the region near the kinematic endpoint. Studies of the impact of various theoretical predictions on the measurements are presented.

Measurements of the total inclusive lepton spectrum in $B \rightarrow X e\nu$ decays have been performed by several experiments operating at the $\Upsilon(4S)$ resonance [2]. The best estimate of this BF has been derived by HFAG [3], based on a global fit to moments of the lepton momentum and hadron mass spectra in $B \rightarrow X e\nu$ decays (corrected for $B \rightarrow X_u e\nu$ decays) either with a constraint on the c-quark mass or by including photon energy moments in $B \rightarrow X_s \gamma$ decays in the fit. Inclusive measurements of $|V_{ub}|$ have been performed at the $\Upsilon(4S)$ resonance, by ARGUS [5], CLEO [6,7], *BABAR* [8] and Belle [9], and experiments at LEP operating at the Z^0 resonance, L3 [10], ALEPH [11], DELPHI [12], and OPAL [13]. Among the $|V_{ub}|$ measurements based on exclusive semileptonic decays [2], the most recent by the LHCb experiment at the LHC is based on the baryon decay $\Lambda_b \rightarrow p\mu\nu$ [14].

This analysis is based on methods similar to the one used in previous measurements of the lepton spectrum near the kinematic endpoint at the $\Upsilon(4S)$ resonance [5,6]. The results presented here supersede the earlier *BABAR* publication [8], based on a partial data sample.

II. DATA SAMPLE

The data used in this analysis were recorded with the *BABAR* detector [15] at the PEP-II energy-asymmetric e^+e^- collider. A sample of 466.5 million $B\bar{B}$ events, corresponding to an integrated luminosity of 424.9 fb^{-1} [16], was collected at the $\Upsilon(4S)$ resonance. An additional sample of 44.4 fb^{-1} was recorded at a center-of-mass (c.m.) energy 40 MeV below the $\Upsilon(4S)$ resonance, i.e., just below the threshold for $B\bar{B}$ production. This off-resonance data sample is used to subtract the non-$B\bar{B}$ background at the $\Upsilon(4S)$ resonance. The relative normalization of the two

data samples has been derived from luminosity measurements, which are based on the number of detected $\mu^+\mu^-$ pairs and the QED cross section for $e^+e^- \rightarrow \mu^+\mu^-$ production, adjusted for the small difference in center-of-mass energy.

III. DETECTOR

The *BABAR* detector has been described in detail elsewhere [15]. The most important components for this study are the charged-particle tracking system, consisting of a five-layer silicon vertex tracker and a 40-layer cylindrical drift chamber, and the electromagnetic calorimeter consisting of 6580 CsI(Tl) crystals. These detector components operated in a 1.5 T magnetic field parallel to the beam. Electron candidates are selected on the basis of the ratio of the energy deposited in the calorimeter to the track momentum, the shower shape, the energy loss in the drift chamber, and the angle of signals in a ring-imaging Cerenkov detector. Showers in the electromagnetic calorimeter with energies below 50 MeV which are dominated by beam background are not used in this analysis.

IV. SIMULATION

We use Monte Carlo (MC) techniques to simulate the production and decay of B mesons and the detector response [17], to estimate signal and background efficiencies, and to extract the observed signal and background distributions. The sample of simulated generic $B\bar{B}$ events exceeds the $B\bar{B}$ data sample by about a factor of 3.

The MC simulations include radiative effects such as bremsstrahlung in the detector material and QED initial and final state radiation [18]. Information from studies of selected control data samples on efficiencies and resolutions is used to adjust and thereby improve the accuracy of the simulation. Adjustments for small variations of the beam energy over time have been included.

In the MC simulations, the BFs for hadronic B and D meson decays are based on values reported in the Review of Particle Physics [2]. The simulation of inclusive charmless semileptonic decays, $B \rightarrow X_u e\nu$, is based on calculations by De Fazio and Neubert (DN) [19]. This simulation produces a continuous mass spectrum of hadronic states X_u. To reproduce and test predictions by other authors this spectrum is reweighted in the course of the analysis. Three-body $B \rightarrow X_u e\nu$ decays with low-mass hadrons, $X_u = \pi, \rho, \omega, \eta, \eta'$, make up about 20% of the total charmless rate. They are simulated separately using the ISGW2 model [20] and added to samples of decays to nonresonant and higher-mass resonant states X_u^{nr}, so that the cumulative distributions of the hadron mass, the momentum transfer squared, and the electron momentum reproduce the inclusive calculation as closely as possible. The hadronization of X_u with masses above $2m_\pi$ is performed according to JETSET [21].

The MC-generated electron momentum distributions for $B \to X_u e \nu$ decays are shown in Fig. 1 for individual decay modes and for their sum. Here and throughout the paper, the electron momentum and all other kinematic variables are measured in the $\Upsilon(4S)$ rest frame, unless stated otherwise. Above 2 GeV/c, the significant signal contributions are from decays involving the light mesons π, ρ, ω, η, and η', in addition to some lower mass nonresonant states X_u^{nr}.

The simulation of the dominant $B \to X_c e \nu$ decays is based on a variety of theoretical prescriptions. For $B \to D e \nu$ and $B \to D^* e \nu$ decays we use form factor parametrizations [22–24], based on heavy quark effective theory. Decays to pseudoscalar mesons are described in terms of one form factor, with a single parameter ρ_D^2. The differential decay rate for $B \to D^* e \nu$ is described by three amplitudes, with decay rates depending on three parameters: $\rho_{D^*}^2$, R_1, and R_2. These parameters have been measured by many experiments; we use the average values presented in Table I.

For the simulation of decays to higher-mass $L = 1$ resonances, D^{**}, i.e., two wide states $D_0^*(2400)$, $D_1'(2430)$, and two narrow states $D_1(2420)$, $D_2^*(2460)$, we have adopted the parametrizations by Leibovich et al. [25] and the HFAG averages [3] for the BFs. For decays to nonresonant charm states $B \to D^{(*)} \pi e \nu$, we rely on the prescription by Goity and Roberts [26] and the BABAR and Belle measurements of the BFs [3]. The simulations of these decays include the full angular dependence of the rate.

The shapes of the MC-generated electron spectra for individual $B \to X_c e \nu$ decays are shown in Fig. 2. Above

TABLE I. Average measured values [3] of the form factor parameters for $B \to D e \nu$ and $B \to D^* e \nu$ decays, as defined by Caprini, Lellouch, and Neubert [23].

	$B \to D e \nu$	$B \to D^* e \nu$
ρ_D^2	1.185 ± 0.054	
$\rho_{D^*}^2$		1.207 ± 0.026
R_1		1.406 ± 0.033
R_2		0.853 ± 0.020

2 GeV/c the dominant contributions are from semileptonic decays involving the lower-mass charm mesons, D and D^*. Higher-mass and nonresonant charm states are expected to contribute at lower electron momenta. The relative contributions of the individual $B \to X_c e \nu$ decay modes have been adjusted to the results of the fit to the observed spectrum (see Sec. VI B 2).

The difference between the measured exclusive decays $B \to (D^{(*)}, D^{**}, D^{(*)}\pi)\ell \nu$ and the inclusive rate for semileptonic B decays to charm final states is $(1.40 \pm 0.28)\%$ [27]. The decay rate for $\bar{B} \to D^{(*)}\pi^+\pi^-\ell^-\bar{\nu}$ was measured by BABAR [28]. Based on these results it was estimated that $\bar{B} \to D^{(*)}\pi\pi\ell^-\bar{\nu}$ decays account for up to half the difference between measured inclusive and the sum of previously measured exclusive branching fractions. Beyond these observed decays, there are missing decay modes, such as $B \to D'(2550)e\nu$ and $B \to D'^*(2600)e\nu$. Candidates for the 2S radial excitations were first observed by BABAR [29] and recently confirmed by LHCb [30]. We have adopted the masses and widths ($130 \pm 18 \,\mathrm{MeV}/c^2$ and $93 \pm 14 \,\mathrm{MeV}/c^2$) measured by BABAR [29], and have simulated these decays using the form factor predictions [27]. Both D^{**} and $D'^{(*)}$ may contribute by their decays to $D^{(*)}\pi\pi$ to $\bar{B} \to D^{(*)}\pi\pi\ell^-\bar{\nu}$
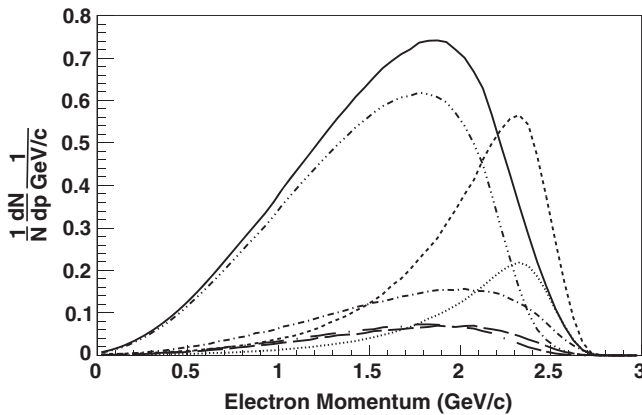

FIG. 1. MC-generated electron momentum spectra in the $\Upsilon(4S)$ rest frame for charmless semileptonic B decays. The full spectrum (solid line) is normalized to 1.0. The largest contribution is from decays involving higher-mass resonances and nonresonant states (X_u^{nr}) (dash-three-dotted). The exclusive decays (scaled by a factor of 5) are $B \to \pi e \nu$ (dash-dotted), $B \to \rho e \nu$ (dashed), $B \to \omega e \nu$ (dotted), $B \to \eta e \nu$ (long-dashed), $B \to \eta' e \nu$ (long-dash-dotted).
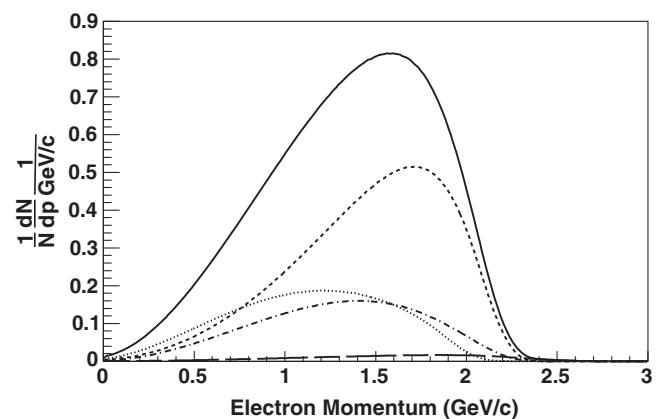

FIG. 2. MC-generated electron momentum spectra for semileptonic decays to charm mesons, $B \to X_c e \nu$ with the total rate (solid line) normalized to 1.0. The individual components are: $B \to D e \nu$ (dash-dotted), $B \to D^* e \nu$ (dashed), $B \to D^{**} e \nu + B \to D^{(*)}\pi e \nu$ (dotted). The highly suppressed $B \to X_u e \nu$ signal spectrum (long dashed) is shown for comparison.

decays. The decay rate for $D_1 \rightarrow D\pi\pi$ was measured by Belle [31] and LHCb [32], LHCb also measured the decay rate for $D_2^* \rightarrow D\pi\pi$. We account for contributions from $\bar{B} \rightarrow D^{**}e^-\bar{\nu}$, $\bar{B} \rightarrow D'^{(*)}e^-\bar{\nu}$, and $\bar{B} \rightarrow D^{(*)}\pi e^-\bar{\nu}$ decays to $\bar{B} \rightarrow D^{(*)}\pi\pi e^-\bar{\nu}$ final states.

The main sources of secondary electrons are semileptonic charm meson decays and $J/\psi \rightarrow e^+e^-$ decays. The J/ψ momentum distribution was determined from this data set and the MC simulation was adjusted to reproduce these measured spectra. The momentum spectra of D and D_s mesons produced in $B\bar{B}$ decays were measured earlier by *BABAR* [33] and the MC simulated spectra were adjusted to reproduce these measurements.

V. CALCULATIONS OF $B \rightarrow X_u\ell\nu$ DECAY RATE

While at the parton level the rate for $b \rightarrow u\ell\nu$ decays can be reliably calculated, the theoretical description of inclusive semileptonic $B \rightarrow X_u\ell\nu$ decays is more challenging. Based on HQE the total inclusive rate can be predicted with an uncertainty of about 5%, however, this rate is very difficult to measure due to very large background from the CKM-favored $B \rightarrow X_c\ell\nu$ decays. On the other hand, in the endpoint region where the signal to background ratio is much more favorable, calculations of the differential decay rates are much more complicated. They require the inclusion of additional perturbative and nonperturbative effects. These calculations rely on HQE and QCD factorization [34] and separate perturbative and nonperturbative effects by using an expansion in powers of $1/m_b$ and a nonperturbative shape function (SF) which is *a priori* unknown. This function accounts for the motion of the b quark inside the B meson, and to leading order, it should be universal for all transitions of a b quark to a light quark [35,36]. It is modeled using arbitrary functions for which low-order moments are constrained by measurable parameters.

For the extraction of $|V_{ub}|$, we rely on $\Delta\mathcal{B}(\Delta p)$, the partial BF for $B \rightarrow X_u e\nu$ decays measured in the momentum interval Δp, and $\Delta\zeta(\Delta p) = \Gamma_{\text{theory}} \times f_u(\Delta p)/|V_{ub}|^2$, the theoretical predictions for partial decay rate normalized by $|V_{ub}|^2$, measured in units of ps^{-1}:

$$|V_{ub}| = \sqrt{\frac{\Delta\mathcal{B}(\Delta p)}{\tau_b \Delta\zeta(\Delta p)}}. \quad (1)$$

Here $\tau_b = (1.580 \pm 0.005)$ ps is the average of the B^0 and B^+ lifetimes [2]. Γ_{theory} is the total predicted decay rate and $f_u(\Delta p)$ refers to the fraction of the predicted decay rate for the momentum interval Δp.

In the following, we briefly describe four different theoretical methods to derive predictions for the partial and total BFs. In the original work by De Fazio and Neubert [19] and Kagan and Neubert [37] the determination of $|V_{ub}|$

relies on the measurement of the electron spectrum for $B \rightarrow X_u e\nu$ and on the radiative decays $B \rightarrow X_s\gamma$ to derive the parameters of the leading SF. More comprehensive calculations were performed by Bosch, Lange, Neubert, and Paz (BLNP) [38–44]. Calculations in the kinetic scheme were introduced by Gambino, Giordano, Ossola, Uraltsev (GGOU) [45,46]. BLNP and GGOU use $B \rightarrow X_c\ell\nu$ and $B \rightarrow X_s\gamma$ decays to derive the parameters of the leading SF. Inclusive spectra for $B \rightarrow X_u e\nu$ decays based on a calculation of nonperturbative functions using Sudakov resummation are presented in the dressed gluon exponentiation (DGE) by Andersen and Gardi [47–50].

We assess individual contributions to the uncertainty of the predictions of the decay rates by the different theoretical approaches. For this purpose, the authors of these calculations have provided software to compute the differential rates and to provide guidance for the assessment of the uncertainties on the rate and thereby $|V_{ub}|$. We differentiate uncertainties originating from the SF parametrization, including the sensitivity to m_b, the b-quark mass, from the impact of the other purely theoretical uncertainties. The uncertainty on m_b, the b-quark mass, has a large impact. Weak annihilation could contribute significantly at high-momentum transfers (q^2). The impact of weak annihilation is generally assumed to be asymmetric, specifically, it is estimated to decrease $|V_{ub}|$ by $O(1–2)\%$ [51].

A. DN calculations

While the calculations by BLNP are to supersede the earlier work by DN, we use DN predictions for comparisons with previous measurements based on these predictions and also for comparisons with other calculations.

The early DN calculations [19] predict the differential spectrum with $O(\alpha_s)$ corrections to leading order in HQE. This approach is based on a parametrization of the leading-power nonperturbative SF. The long-distance interaction is described by a single light-cone distribution. In the region close to phase-space boundaries these nonperturbative corrections to the spectrum are large. The prediction for the decay distribution is obtained by a convolution of the parton model spectrum with the SF. The SF is described by two parameters $\bar{\Lambda}^{\text{SF}} = M_B - m_b$ and λ_1^{SF} which were determined from the measured photon energy moments in $B \rightarrow X_s\gamma$ decays [37]. We use *BABAR* measurements [52] of the SF parameters, $m_b^{\text{SF}} = (4.79^{+0.06}_{-0.10})$ GeV and $\lambda_1^{\text{SF}} = -0.24^{+0.09}_{-0.18}$ GeV^2 with 94% correlation.

DN predict the shape of the differential electron spectrum, but they do not provide a normalization. Thus to determine the partial rates $\Delta\zeta(\Delta p)$, we rely on the DN predictions for $f_u(\Delta p)$, the fractions of $B \rightarrow X_u e\nu$ decays in the interval Δp, and an independent prediction for the normalized total decay rate $\zeta = (65.7^{+2.4}_{-2.7})$ ps^{-1} [48] [the current value of $m_b^{\overline{\text{MS}}} = (4.18 \pm 0.03)$ GeV [2] is used to

calculate ζ]. Earlier determinations of ζ can be found in [51,53–58].

The uncertainty on $|V_{ub}|$ due to the application of the shape function is derived from 10% variations of $\bar{\Lambda}^{SF}$ and λ_1^{SF}, as prescribed by the authors. The estimated total theoretical uncertainty on $|V_{ub}|$ is about 2.1% (for $p_e > 0.8$ GeV/c).

B. BLNP predictions

The BLNP calculations incorporate all known perturbative and power corrections and interpolation between the HQE and SF regions [38–40]. The differential and partially integrated spectra for the inclusive $B \to X_u l\nu$ decay are calculated in perturbative theory at next-to-leading order (NLO) in renormalization-group, and at the leading power in the heavy quark expansion. Formulas for the triple differential rate of $B \to X_u l\nu$ and for the $B \to X_s\gamma$ photon spectrum are convolution integrals of weight functions with the shape function renormalized at the intermediate scale μ_i. The ansatz for the leading SF depends on two parameters, m_b and μ_π^2; subleading SFs are treated separately.

The SF parameters in the kinetic scheme are determined by fits to moments of the hadron mass and lepton energy spectra from inclusive $B \to X_c\ell\nu$ decays and either additional photon energy moments in $B \to X_s\gamma$ decays or by applying a constraint on the c-quark mass, $m_c^{\overline{MS}}(3 \text{ GeV}) = 0.998 \pm 0.029 \text{ GeV}/c^2$. These parameters are translated from the kinetic to the SF mass scheme [42].

The impact of the uncertainties in these SFs are estimated by varying the scale parameters μ_i and choices of different subleading SF. The next-to-next-to-leading order (NNLO) corrections were studied in detail [44]. In extractions of $|V_{ub}|$, the choice $\mu_i = 1.5$ GeV introduces for the NNLO corrections significant shifts to lower values of the partial decay rates, by $\sim$15%–20%, while at the same time reducing the perturbative uncertainty on the scale μ_h. At NLO, small changes of the value of μ_i impact the agreement between the NLO and NNLO results. We adopt the authors' recommendation and use values $\mu_i = 2.0$ GeV and $\mu_h = 4.25$ GeV, as the default. The results obtained in the SF mass scheme with the m_c constraint and $\mu_i = 2.0$ GeV are $m_b^{SF} = (4.561 \pm 0.023)$ GeV and $\mu_\pi^{2SF} = (0.149 \pm 0.040)$ GeV^2 [59]. The 1σ contours for different choices of these parameters are presented in Fig. 3.

In the BLNP framework, the extraction of $|V_{ub}|$ is based on the predicted partial rate $\zeta(\Delta p)$ [43] for $B \to X_u e\nu$ decays and the measurement of $\Delta \mathcal{B}$. The predictions for total decay rate are

$$\zeta = (73.5 \pm 1.9_{SF}{}^{+5.5}_{-4.9\,\text{theory}}) \text{ ps}^{-1}$$
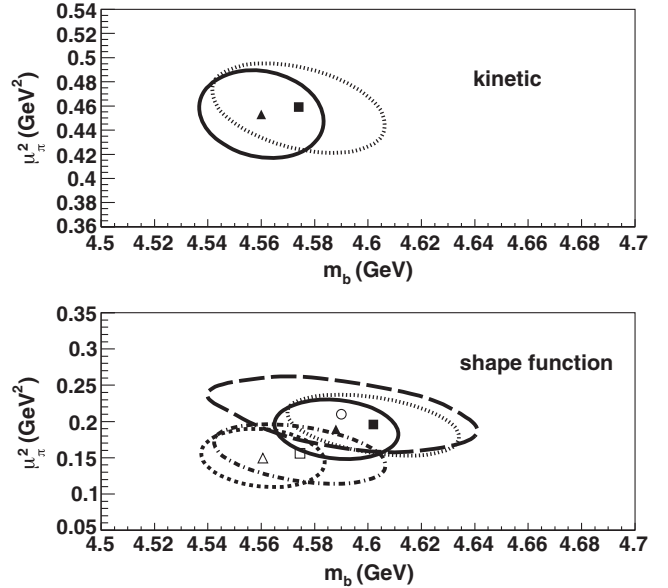$$m_c \text{ constraint}, \quad \mu_i = 2.0 \text{ GeV}, \quad (2)$$

FIG. 3. The shape function parameters m_b and μ_π^2 in the kinetic scheme (HFAG 2014): fit to X_c data with constraint on the c-quark mass (solid line, solid triangle); fit to $X_c + X_s\gamma$ data ($\mu_i = 1.5$ GeV, $\mu = \mu_i$) (dotted line, solid square). Translation of fit to X_c data with constraint on the c-quark mass (short dashed line, open triangle); translation of fit to $X_c + X_s\gamma$ data with $\mu_i = 2.0$ GeV, $\mu = \mu_i$ (dash-dotted line, open square). The previous *BABAR* endpoint analysis [8] was based on a $X_s + X_c$ fit (long dashed line, open circle). The contours represent $\Delta\chi^2 = 1$.

$$\zeta = (70.4 \pm 1.9_{SF}{}^{+6.4}_{-5.2\,\text{theory}}) \text{ ps}^{-1}$$
$$m_c \text{ constraint}, \quad \mu_i = 1.5 \text{ GeV}, \quad (3)$$

$$\zeta = (74.5 \pm 2.7_{SF}{}^{+5.5}_{-4.9\,\text{theory}}) \text{ ps}^{-1}$$
$$X_s\gamma \text{ constraint}, \quad \mu_i = 2.0 \text{ GeV}, \quad (4)$$

$$\zeta = (71.4 \pm 2.7_{SF}{}^{+6.5}_{-5.3\,\text{theory}}) \text{ ps}^{-1}$$
$$X_s\gamma \text{ constraint}, \quad \mu_i = 1.5 \text{ GeV}. \quad (5)$$

The estimated SF uncertainty and total theoretical uncertainty on $|V_{ub}|$ are about 5.0% and 3.6%, respectively (for $p_e > 0.8$ GeV/c).

C. GGOU predictions

The GGOU calculations [45,46] of the triple differential decay rate include all perturbative and nonperturbative effects through $O(\alpha_s^2\beta_0)$ and $O(1/m_b^3)$. The Fermi motion is parametrized in terms of a single light-cone function for each structure function and for any value of q^2, accounting for all subleading effects. The calculations are based on the kinetic mass scheme, with a hard cutoff at $\mu = 1$ GeV.

The SF parameters are determined by fits to moments of the hadron mass and lepton energy spectra from inclusive $B \to X_c \ell \nu$ decays, and either including photon energy moments in $B \to X_s \gamma$ decays or by applying a constraint on the c-quark mass. The results obtained in the kinetic scheme with the m_c constraint are $m_b^{\text{kin}}(1.0 \text{ GeV}) = (4.560 \pm 0.023) \text{ GeV}$ and $\mu_\pi^{2\,\text{kin}}(1.0 \text{ GeV}) = (0.453 \pm 0.036) \text{ GeV}^2$ [59]. The 1σ contours for the resulting SF parameters are presented in Fig. 3.

The uncertainties are estimated as prescribed in [46]. To estimate the uncertainties of the higher order perturbative corrections, the hard cutoff is varied in the range $0.7 < \mu < 1.3$ GeV. Combined with an estimate of 40% of the uncertainty in $\alpha_s^2 \beta_0$ corrections, this is taken as the overall uncertainty of these higher order perturbative and nonperturbative calculations. The uncertainty due to weak annihilation is assumed to be asymmetric, i.e., it tends to decrease $|V_{ub}|$. The uncertainty in the modeling of the tail of the q^2 distribution is estimated by comparing two different assumptions for the range (8.5–13.5) GeV^2.

The extraction of $|V_{ub}|$ is based on the measured partial BF $\Delta\mathcal{B}(\Delta p)$, and the GGOU prediction for the partial normalized rate $\zeta(\Delta p)$. The predictions for the total decay rate are

$$\zeta = (67.2 \pm 1.6_{\text{SF}}{}^{+2.5}_{-1.3\,\text{theory}}) \text{ ps}^{-1}$$
$$m_c \text{ constraint}, \tag{6}$$

$$\zeta = (67.9 \pm 2.3_{\text{SF}}{}^{+2.8}_{-5.1\,\text{theory}}) \text{ ps}^{-1}$$
$$X_s\gamma \text{ constraint}. \tag{7}$$

The estimated uncertainties on $|V_{ub}|$ for the SF and the total theoretical uncertainty are about 4.1% and 2.0%, respectively (for $p_e > 0.8$ GeV/c).

D. DGE predictions

The DGE [47] is a general formalism for inclusive distributions near the kinematic boundaries. In this approach, the on-shell calculation, converted to hadronic variables, is directly used as an approximation to the decay spectrum without the use of a leading-power nonperturbative function. The perturbative expansion includes NNLO resummation in momentum space as well as full $O(\alpha_s)$ and $O(\alpha_s^2 \beta_0)$ corrections. The triple differential rate of $B \to X_u l \nu$ was calculated [48,50]. The DGE calculations rely on the $\overline{\text{MS}}$ renormalization scheme.

Based on the prescriptions by the authors [50], we have estimated the uncertainties in these calculations and their impact on $|V_{ub}|$. The theoretical uncertainty is obtained by accounting for the uncertainty in $\alpha_s = 0.1184 \pm 0.0007$ and $m_b^{\overline{\text{MS}}} = (4.18 \pm 0.03)$ GeV [2]. The renormalization scale factor $\mu/m_b = 1.0$ is varied between 0.5 and 2.0, and the default values of $(C_{3/2}, f^{pv}) = (1.0, 0.0)$ are changed

to $(C_{3/2}, f^{pv}) = (6.2, 0.4)$ to assess the uncertainties in the nonperturbative effects.

DGE predict the shape of differential electron spectrum, but do not provide a normalization. Thus we rely on the DGE predictions for $f_u(\Delta p)$, the fraction of $B \to X_u e \nu$ decays in the interval Δp, and an independent prediction for the normalized total decay rate, $\zeta = (65.7^{+2.4}_{-2.7})$ ps^{-1} [48] to derive $\Delta\zeta(\Delta p)$ [the current value of $m_b^{\overline{\text{MS}}} = (4.18 \pm 0.03)$ GeV [2] is used to calculate ζ].

The estimated total theoretical uncertainty on $|V_{ub}|$ for DGE calculations is about 2.2% (for $p_e > 0.8$ GeV/c).

VI. ANALYSIS

A. Event Selection

To select $B\bar{B}$ events with a candidate electron from a semileptonic B meson decay, we apply the following criteria:
Electron selection: We select events with at least one electron candidate in the c.m. momentum range $0.8 < p_{\text{cms}} < 5.0$ GeV/c and within the polar angle acceptance in the laboratory frame of $-0.71 < \cos\theta_e < 0.90$. Within these constraints the identification efficiency for electrons exceeds 94%. The average hadron misidentification rate is about 0.1%.
Track multiplicity: To suppress background from non-$B\bar{B}$ events, primarily low-multiplicity QED processes, including $\tau^+\tau^-$ pair production and $e^+e^- \to q\bar{q}(\gamma)$ annihilation (q represents a u, d, s or c quark), we reject events with fewer than four charged tracks.
J/ψ suppression: To reject electrons from the decay $J/\psi \to e^+e^-$, we combine the selected electron with other electron candidates of opposite charge and reject the event if the invariant mass of any pair is consistent with a J/ψ decay, $3.00 < m_{e^+e^-} < 3.15$ GeV/c^2.
If an event in the remaining sample has more than one electron that passes this selection, the one with the highest momentum is chosen as the signal candidate.

To further suppress non-$B\bar{B}$ events we build a neural network (NN) with the following input variables which rely on the momenta of all charged particles and energies of photons above 50 MeV detected in the event:
(i) $\mathcal{R}_2$, the ratio of the second to the zeroth Fox-Wolfram moments [60], calculated from all detected particles in the event [Fig. 4(a)].
(ii) $l_2 = \sum_i p_i \cos^2\theta_i / 2E_{\text{beam}}$, where the sum includes all detected particles except the electron, and θ_i is the angle between the momentum of particle i and the direction of the electron momentum [Fig. 4(b)].
(iii) $\cos\theta_{e-\text{roe}}$, the cosine of the angle between the electron momentum and the axis of the thrust of the rest of the event [Fig. 4(c)].

The distribution of the NN output is shown in Fig. 5. Only events with positive output values are retained, this selects ∼90% of $B \to X_u e \nu$ and ∼20% non-$B\bar{B}$ events. The positive output corresponds the selection with maximum significance level.

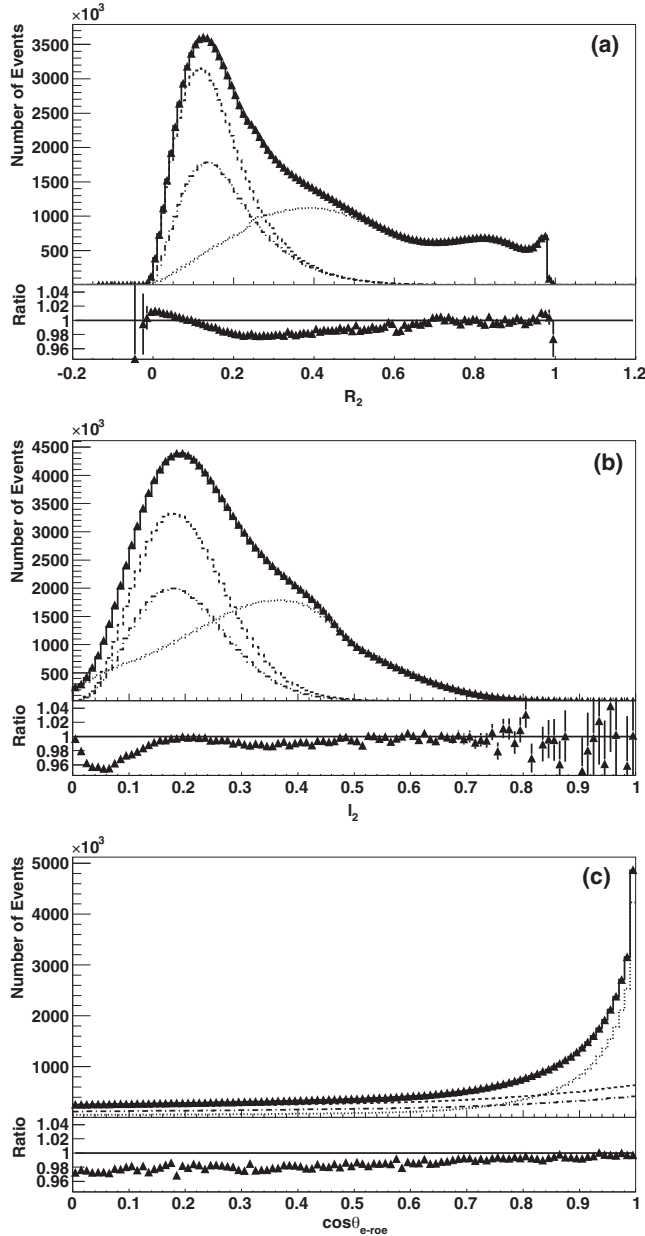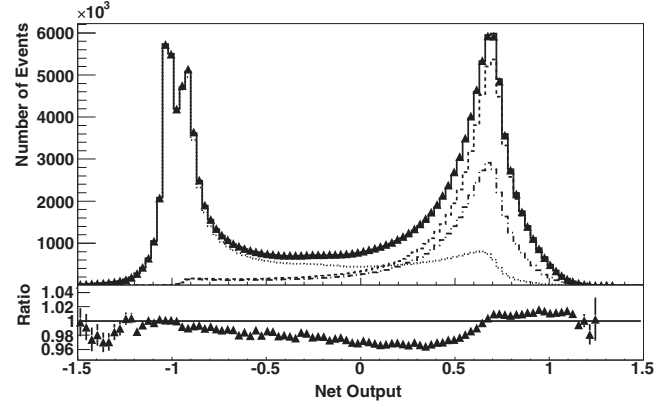FIG. 5.   The distribution of events as a function of the NN output: On-resonance data (triangles), the sum of MC simulated $B\bar{B}$ and off-resonance data (solid histogram), MC simulated $B\bar{B}$ events (dashed histogram), off-resonance data (dotted histogram). For comparison, the distributions for $B\bar{B}$ events with a signal $B \to X_u e\nu$ decay (dash-dotted histogram) are shown (scaled by a factor of 50). Ratio $= [B\bar{B}\,(\mathrm{MC}) + \mathrm{off\text{-}resonance}]/\mathrm{on\text{-}resonance}$.

FIG. 4.   The number of events before the NN selection, as a function of (a) $\mathcal{R}_2$, (b) l_2, (c) $\cos\theta_{e-\mathrm{roe}}$: on-resonance data (triangles), the sum of simulated $B\bar{B}$ events and off-resonance data (solid histogram), MC simulated $B\bar{B}$ events (dashed histogram), and off-resonance data (dotted histogram). For comparison, the distributions for $B\bar{B}$ events with a signal $B \to X_u e\nu$ decay (dash-dotted histogram), are shown (scaled by a factor of 50). Ratio $= [B\bar{B}\,(\mathrm{MC}) + \mathrm{off\text{-}resonance}]/\mathrm{on\text{-}resonance}$.

This selection results in an efficiency of 50%–60% for $B \to X_u e\nu$ decays; the dependence on the electron momentum is shown in Fig. 6.

B. Background subtraction

The selected sample of events from the on-resonance data contains considerable background from $B\bar{B}$ events and

non-$B\bar{B}$ events. The $B\bar{B}$ background is dominated by primary electrons from semileptonic B decays and secondary electrons from decays of charm mesons and J/ψ mesons. Hadronic B decays contribute mostly via the misidentification of charged particles. Non-$B\bar{B}$ events originate from $e^+e^- \to q\bar{q}(\gamma)$ annihilation and lepton pair production, especially $e^+e^- \to \tau^+\tau^-$.

1. Non-$B\bar{B}$ background

To determine the momentum-dependent shape of the non-$B\bar{B}$ background, we perform a binned χ^2 fit to the off-resonance data in the momentum interval 0.8 to 3.5 GeV/c, combined with on-resonance data in the momentum interval 2.8 to 3.5 GeV/c, i.e., above the endpoint for electrons from B decays. Since the c.m. energy for the off-resonance data is 0.4% lower than for the on-resonance data, we scale the electron momenta for the off-resonance data by the ratio of the c.m. energies.

The relative normalization for the two data samples [15,16] is

$$r_L^{(0)} = \frac{s_{\mathrm{OFF}}}{s_{\mathrm{ON}}} \frac{\int L_{\mathrm{ON}}dt}{\int L_{\mathrm{OFF}}dt} = 9.560 \pm 0.003_{\mathrm{stat}} \pm 0.006_{\mathrm{syst}},$$

where s and $\int L dt$ refer to the c.m. energy squared and integrated luminosity of the on- and off-resonance data. The statistical uncertainty of r_L of 0.03% is based on the number of detected $\mu^+\mu^-$ pairs used for the measurement of the integrated luminosity; the relative systematic uncertainty on the ratio is estimated to be 0.06%.

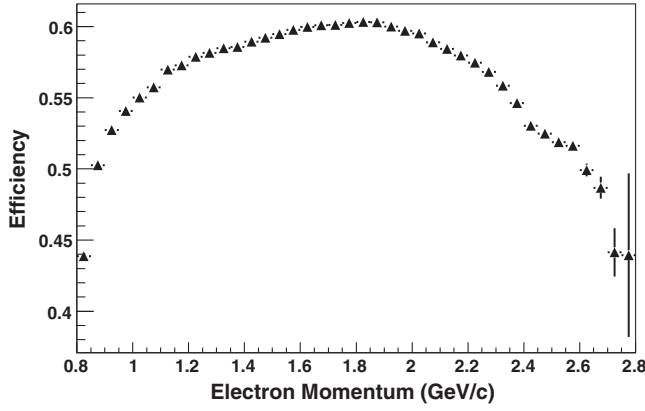The binned χ^2 for the fit to the electron spectrum for selected non-$B\bar{B}$ events is defined as

FIG. 6.   Selection efficiency for $B\bar{B}$ events with a $B \to X_u e\nu$ decay as a function of the MC-generated electron momentum. The error bars represent the statistical uncertainties only.

$$\chi_c^2 = \sum_{p_i > 0.8 \text{ GeV}/c} \frac{(f(\vec{a}, p_i) - r_L n_i)^2}{r_L^2 n_i}$$

$$+ \sum_{p_j > 2.8 \text{ GeV}/c} \frac{(f(\vec{a}, p_j) - N_j)^2}{N_j} + \frac{(r_L - r_L^{(0)})^2}{\sigma_{r_L}^2}. \qquad (8)$$

Here n_i and N_j refer to the number of selected events in the off- and on-resonance samples for momentum bins i and j, respectively, $\vec{a}$ represents the set of free parameters of the fit, and σ_{r_L} is the uncertainty on $r_L^{(0)}$. To fit the momentum spectrum, we have chosen an exponential expression of the form,

$$f(\vec{a}, p) = a_0(\exp(a_1 p + a_2 p^2 + a_3 p^3)$$

$$+ \exp(a_4 p + a_5 p^2)). \qquad (9)$$

We perform three different fits and they all describe the data well, see Table II. The results of the fit to both on- and off-resonance data are shown in Fig. 7. In the fit to the full on-resonance data spectrum, the constraint on the ratio $r_L/r_L^{(0)} = 1.0000 \pm 0.0007$ is applied.

In Fig. 8(a) the data and the result of this fit to the non-$B\bar{B}$ background are compared to the full spectrum of the highest momentum electron in selected events observed in the on-resonance data sample. By subtracting the fitted non-$B\bar{B}$ background we obtain the inclusive electron spectrum from $\Upsilon(4S)$ decays, shown in Fig. 8(b). Above

TABLE II.   Results of the fit to the non-$B\bar{B}$ background.

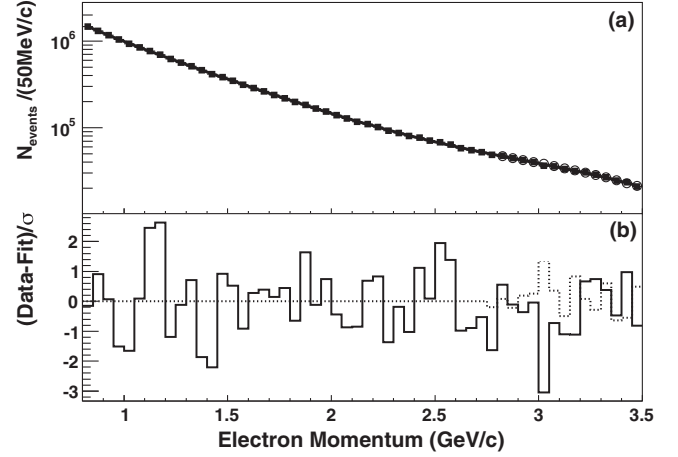| Data	$\chi^2/N_{\text{d.o.f.}}$	$r_L/r_L^{(0)}$
Off-resonance only	65.0/48	
Off- and on-resonance	70.6/61	1.007 ± 0.004
Off- and on-resonance with $r_L/r_L^{(0)}$ constrained	73.0/62	1.0002 ± 0.0007

FIG. 7.   The combined fit to off-resonance data in the momentum interval of 0.8 to 3.5 GeV/c and to on-resonance data in the momentum interval of 2.8 to 3.5 GeV/c, with the constraint on $r_L/r_L^{(0)}$; (a) comparison of off-resonance data (solid squares), on-resonance data (open circles) and fitted function; (b) (Data Fit)/σ: off-resonance data (solid histogram), on-resonance data (dotted histogram)

2.3 GeV/c, an excess of events corresponding to the expected signal $B \to X_u e\nu$ decays is observed above the $B\bar{B}$ background.

2. $B\bar{B}$ Background and fit to the electron spectrum

The $B\bar{B}$ background spectrum is composed of several contributions, dominated by primary electrons from various semileptonic B decays, and secondary electrons from decays of D, D_s, and J/ψ mesons or photon
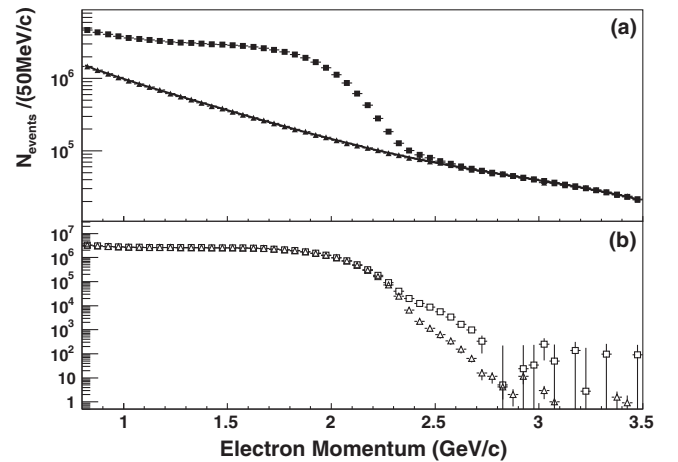

FIG. 8.   Electron momentum spectra in the $\Upsilon(4S)$ rest frame: (a) on-resonance data (solid squares), scaled off-resonance data (solid triangles), the solid line shows the results of the fit to the continuum component using both on-resonance and off-resonance data. (b) On-resonance data with non-$B\bar{B}$ background subtracted (open squares), $B\bar{B}$ MC without $B \to X_u e\nu$ decays (open triangles).

conversions. Hadronic B decays contribute mostly via charged-particle misidentification, primarily at low momenta. The MC simulated contributions from different background sources are shown in Fig. 9.

We estimate the total background by a simultaneous fit to the observed inclusive electron spectra in off- and on-resonance data to the sum of the signal and individual background contributions. For the individual signal and $B\bar{B}$ background contributions, we rely on the MC simulated shapes of the spectra (including some corrections), and treat their relative normalization as free parameters in the fit. For this extended fit, we expand the χ^2 definition as follows:

$$\chi^2 = \sum_{i,j}(f(\vec{a}, p_i) + S(\vec{b}, \vec{t}, p_i) - N_i)V_{ij}^{-1}$$
$$\times (f(\vec{a}, p_j) + S(\vec{b}, \vec{t}, p_j) - N_j)$$
$$+ \sum_i \frac{(f(\vec{a}, p_i) - r_L n_i)^2}{r_L^2 n_i}$$
$$+ \sum_k \frac{(b_k - b_k^{(0)})^2}{\sigma_{b_k}^2} + \frac{(r_L - r_L^{(0)})^2}{\sigma_{r_L}^2}, \qquad (10)$$

with

$$V_{ij} = (N_i + \sigma_{(MC)i}^2)\delta_{ij} + V_{ij}^{PID}.$$

Here n_i and N_j refer to the number of selected events in the off- and on-resonance samples for momentum bins i and j, respectively, and $\vec{a}$ is the set of free parameters of the fit.

The first sum refers to the on-resonance data. The $B\bar{B}$ electron spectrum is approximated as $S(\vec{b}, \vec{t}, p) = \sum_k b_k g_k(\vec{t}, p_i)$, where the free parameters b_k are the BFs for the individual contributions $g_k(\vec{t}, p_j)$ representing the signal $B \to X_u e\nu$ decays, the background of primary electrons from semileptonic B decays ($De\nu$, $D^* e\nu$, $D^{(*)}\pi e\nu$, $D^{**} e\nu$ and $D'^{(*)} e\nu$), and secondary electrons from decays of D and D_s mesons ($D, D_s \to e$ fitted as a scale factor relative to the MC input). Smaller contributions to the $B\bar{B}$ background are fixed in the fit, for example, electrons from J/ψ and $\tau^\pm$ decays, photon conversions, and hadrons misidentified as electrons. Their simulations and rates rely on independent control samples and are well understood.

The momentum spectra $g_k(\vec{t}, p_j)$ are histograms taken from MC simulations. The array $\vec{t}$ refers to the form factor parameters ρ_{D*}^2, R_1, R_2, and ρ_D^2 and other fixed parameters such as form factor parameters for $B \to D^{**} e\nu$ and $B \to D'^{(*)} e\nu$ decays. $\sigma_{(MC)j}$ is the statistical uncertainty of the number of simulated events in the jth bin. V_{ij}^{PID} is the covariance matrix for the detection of electrons among charged tracks. It includes electron identification and
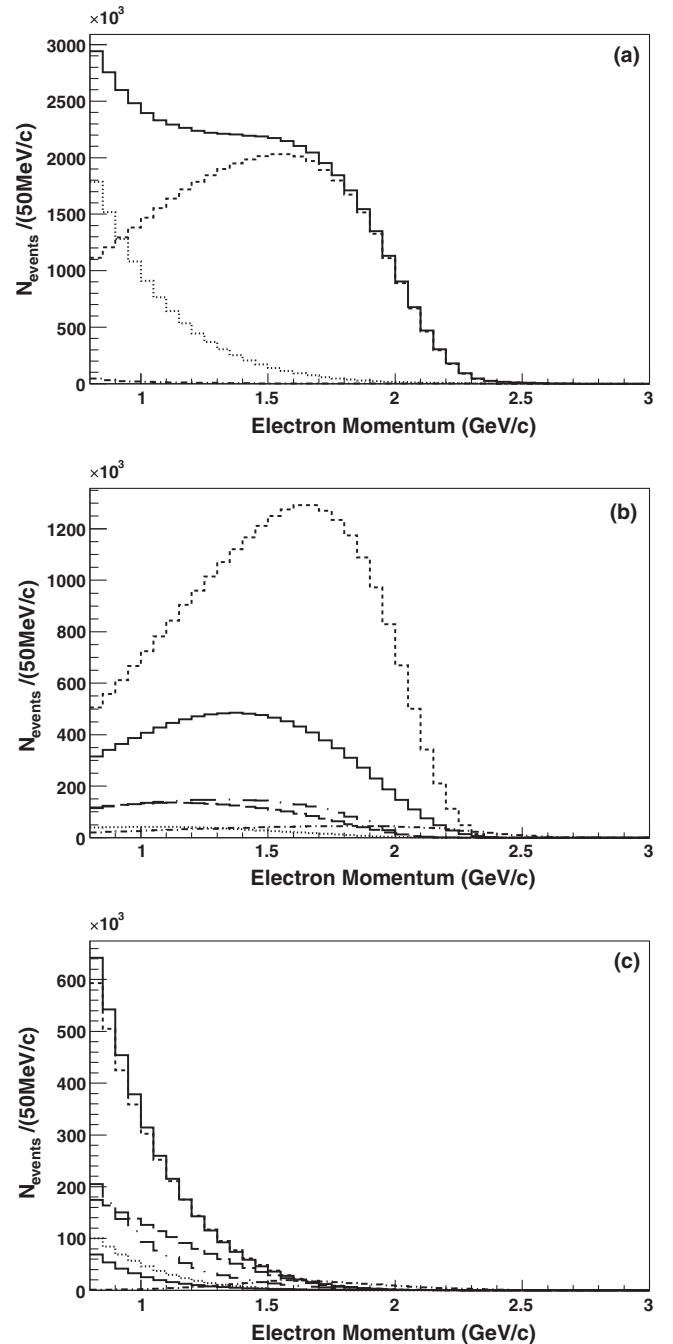

FIG. 9. The simulated contributions to $B\bar{B}$ events as a function of the momentum for electron candidates (a) all events (solid histogram), primary electrons (dashed histogram), secondary electrons (dotted histogram), misidentified hadrons (dash-dotted histogram). (b) Primary electrons: $B \to De\nu$(solid histogram), $B \to D^* e\nu$ (dashed histogram), $B \to D^{(*)}\pi e\nu$ (dotted histogram), $B \to (D_0^* + D_1^*)e\nu$ (long-dashed histogram), $B \to (D_1 + D_2^*)e\nu$ (long-dash-dotted histogram), signal $B \to X_u e\nu$ decays (dash-dotted histogram). (c) Secondary electrons from $D^\pm$ (solid histogram), $D^0(\bar{D}^0)$ (dashed histogram), D_s (dotted histogram), J/ψ (dash-dotted histogram), τ (long-dashed histogram), γ conversion (long-dash-dotted histogram), other $e^\pm$ (dash-three-dotted histogram).

TABLE III.   Results of the fit to the electron spectrum, with the non-$B\bar{B}$ background subtracted and with all entries in the interval from 2.1 to 2.7 GeV/c in a single bin, for four different theoretical predictions of the $X_u e\nu$ spectrum. Fitted BFs(%), averaged over charged and neutral B mesons, for the signal $X_u e\nu$, the background $De\nu$ (constrained), $D^* e\nu$, $D^{(*)}\pi e\nu$, $D^{**} e\nu$, $D'(2.55)e\nu + D'^*(2.60)e\nu$, and scale factors relative to reweighted MC inputs for secondary $D \to e$, and the luminosity ratio r_L (constrained) are presented. The contributions to the χ^2 from the on-resonance and the off-resonance data and constraints, and the ratio of the total χ^2 per degree of freedom are listed at the bottom.

	DN	BLNP$_{\mu_i = 2.0 \text{ GeV}}$ m_c constraint	GGOU m_c constraint	DGE
$X_u e\nu$	0.149 ± 0.005	0.240 ± 0.008	0.166 ± 0.006	0.153 ± 0.005
$De\nu$	2.233 ± 0.090	2.197 ± 0.088	2.226 ± 0.089	2.230 ± 0.089
$D^* e\nu$	5.612 ± 0.049	5.424 ± 0.049	5.579 ± 0.048	5.611 ± 0.048
$D^{(*)}\pi e\nu$	<0.052	<0.025	<0.050	<0.075
$D^{**} e\nu$	2.285 ± 0.071	2.540 ± 0.075	2.331 ± 0.070	2.287 ± 0.070
$D'^{(*)} e\nu$	0.046 ± 0.011	0.023 ± 0.011	0.041 ± 0.011	0.045 ± 0.011
$D \to e$	0.982 ± 0.005	0.968 ± 0.005	0.980 ± 0.005	0.982 ± 0.005
$r_L / r_L^{(0)}$	1.0002 ± 0.0007	1.0002 ± 0.0007	1.0002 ± 0.0007	1.0002 ± 0.0007
$\chi^2_{\text{ON}} + \chi^2_{\text{OFF}} + \chi^2_{\text{constraints}}$	$27.4 + 69.7 + 0.1$	$31.9 + 70.9 + 0.2$	$27.8 + 69.9 + 0.1$	$26.8 + 69.7 + 0.1$
$\chi^2 / N_{\text{d.o.f.}}$	$97.2/85$	$102.9/85$	$97.8/85$	$96.6/85$

misidentification of pions, kaons, protons and antiprotons, studied with large data control samples. V_{ij}^{PID} only includes the uncertainty for the shape of the momentum distribution due to particle identification (PID) uncertainties. The uncertainty of the relative normalization due to PID uncertainties is about 0.5% and is taken as a systematic uncertainty. The last two terms of Eq. (10) refer to quantities that are well known.

In the fit, $De\nu$ and $D^{**} e\nu$ contributions are highly correlated. The BF for $B \to De\nu$ is constrained to 0.022 ± 0.001 [2]. The luminosity ratio is constrained to the value $r_L^{(0)} = 9.560 \pm 0.007$ [15,16].

The fit is performed in the momentum range from 0.8 to 3.5 GeV/c, in bins of 50 MeV/c. At lower momenta, the data determine the relative normalization of the various background contributions, allowing for an extrapolation of these backgrounds into the endpoint region. This fitting procedure was chosen in recognition of the fact that the current BFs for the individual $B \to X_c \ell \nu$ decays are not sufficiently well measured to perform an adequate background subtraction. The shape of the signal spectrum is fixed in the fit to one of the theoretical predictions, its normalization is a free parameter. In a given momentum interval, the excess of events above the sum of the fitted backgrounds is taken as the number of signal events.

To reduce a potential systematic bias from the theoretically predicted shape of the signal spectrum in a region where these calculations are less reliable, events in the interval from 2.1 to 2.7 GeV/c are combined into a single bin. The lower limit of this bin is chosen so as to retain sensitivity to the steeply falling $B\bar{B}$ background distributions, while containing a large fraction of the signal events in a region where the background is low. The upper limit at 2.7 GeV/c is chosen to limit the non-$B\bar{B}$ background at

higher momenta where the signal contributions become very small compared to the non-$B\bar{B}$ background.

The fits are performed separately for the different theoretical predictions of the signal spectrum, introduced in Sec. V. The results of these fits are shown in Table III, and for the fit with the GGOU signal spectrum, the correlation matrix is presented in Table IV. The differences of the correlation matrices for the fit with DN, BLNP, GGOU and DGE signal spectra are small. The difference in the fit results for the $B \to X_u e\nu$ BF is primarily due to the difference between the various predictions for the fraction of the signal spectrum in the high-momentum range. The fitted BFs for the dominant $B \to X_c e\nu$ decays agree reasonably well with expectations [2].

Since the ability of the fit to distinguish between individual $D^{**} e\nu$ decay modes is limited, the sum of the four measured decay modes ($D_0^* e\nu$, $D_1' e\nu$, $D_1 e\nu$, $D_2^* e\nu$) is treated as single contribution in the fit, with the relative BFs for the individual components fixed. Similarly, the contributions from $B \to D' e\nu$ and $B \to D'^* e\nu$ are added, and the sum is treated as single contribution, with the relative BFs for the two components fixed.

VII. SYSTEMATIC UNCERTAINTIES

The principal sources of systematic uncertainties in the measurement of the lepton spectrum from $B \to X_u e\nu$ decays are the following:
 (i) the signal selection,
 (ii) the simulation of the signal electron spectrum,
 (iii) the subtraction of the non-$B\bar{B}$ background,
 (iv) the subtraction of the $B\bar{B}$ background.

To estimate the systematic uncertainties on the signal electron spectrum and BFs, we compare the result obtained from the nominal fit with results obtained after changes to

TABLE IV. Correlation matrix for the fit to the total electron spectrum with the GGOU prediction of the signal spectrum, with the contributions to the spectrum and the parameters of the background function, a_0 through a_5.

	$De\nu$	$D^*e\nu$	$D^{(*)}\pi e\nu$	$D^{**}e\nu$	$D'^{(*)}e\nu$	$X_u e\nu$	$D \to e$	a_0	a_1	a_2	a_3	a_4	a_5	$r_L/r_L^{(0)}$
$De\nu$	1	−0.827	0.032	−0.398	−0.449	−0.305	−0.060	0.018	−0.048	0.058	−0.036	0.023	−0.032	0.001
$D^*e\nu$		1	−0.024	−0.158	0.784	−0.128	0.309	0.050	0.029	−0.146	0.126	0.038	0.125	0.008
$D^{(*)}\pi e\nu$			1	−0.031	0.004	0.027	0.012	−0.066	0.033	0.033	−0.048	−0.044	−0.052	−0.028
$D^{**}e\nu$				1	−0.601	0.598	−0.361	−0.062	0.030	0.055	−0.063	−0.055	−0.066	−0.012
$D'^{(*)}e\nu$					1	−0.236	0.206	0.069	−0.051	−0.034	0.053	0.070	0.063	0.001
$X_u e\nu$						1	−0.252	−0.461	0.310	0.252	−0.369	−0.425	−0.363	−0.107
$D \to e$							1	−0.108	0.204	−0.189	0.104	−0.102	0.037	−0.116
a_0								1	−0.827	−0.196	0.670	0.980	0.671	0.139
a_1									1	−0.315	−0.190	−0.870	−0.209	−0.103
a_2										1	−0.801	−0.122	−0.818	0.012
a_3											1	0.610	0.947	0.035
a_4												1	0.627	0.027
a_5													1	−0.006
$r_L/r_L^{(0)}$														1

the MC simulation that reflect the uncertainty in the parameters that impact the detector efficiency and resolution, or the simulation of the signal and background processes. The sensitivity to the detailed description of the inclusive signal spectrum, in particular the theoretical uncertainties in the QCD corrections will be discussed in Sec. VIII.

A summary of the experimental systematic uncertainties is given in Table V for four intervals of the electron momentum with different lower limits, and a common upper limit of 2.7 GeV/c. The uncertainty in the simulation of the detector performance and its impact on the momentum dependence of the efficiencies for signal and background are the experimental limitations of the current analysis. The largest source of uncertainties in the fit to the observed electron spectrum, is the event selection, primarily the suppression of the non-$B\bar{B}$ background using a neural network. The impact of the uncertainties in the theoretical predictions of the spectrum are not included in this Table.

A. Event selection

The principal sources of uncertainties in the event selection arise from the efficiency of reconstruction of charged-particle tracks, the restriction on the number of charged particles, the electron identification, and the application of a neural network.

The single charged-particle tracking efficiency inside the detector acceptance exceeds 96% and it is largely independent of momentum. It is well reproduced by the MC simulation. To estimate the impact of the uncertainty in the detection of charged-particle tracks, the track finding efficiency is decreased by 1 standard deviation (σ) and the fit is repeated. The observed impact is 0.1% for electron momenta below 2.3 GeV/c and increases slightly at higher momenta.

The electron identification efficiency has been studied on a high statistics sample of radiative Bhabha events, with electron momenta in the laboratory frame extending up to 10 GeV/c. The ratio of efficiencies from Bhabha data and

TABLE V. Summary of the relative systematic uncertainties (%) on the partial branching fraction measurements for $B \to X_u e\nu$ decays (GGOU), as a function of $p^{\min}$, the lower limit of the signal momentum range, the upper limit is fixed at 2.7 GeV/c. The uncertainties in the theoretical predictions of the signal spectrum are not included here.

$p^{\min}$ (GeV/c)	0.8	1.5	2.1	2.3
Single Track efficiency	0.1	0.1	0.1	0.0
Charged track multiplicity	1.2	1.9	1.3	1.0
Particle identification	0.5	0.5	0.5	0.5
Hadron mis-ID background	0.7	0.7	0.8	0.5
Photon selection	0.4	0.3	0.4	0.2
Neural net event selection	$^{+3.0}_{-0.8}$	$^{+3.3}_{-1.2}$	$^{+3.6}_{-1.2}$	$^{+3.1}_{-2.1}$
Non-$B\bar{B}$ background	0.5	0.5	0.5	0.8
$B \to X_u e\nu$ exclusive decays	0.3	0.3	0.3	0.3
$B \to D^{(*)}l\nu$ form factors	1.1	0.5	1.2	0.2
$B \to D^{**}e\nu$ form factors	0.6	0.4	0.6	0.0
$B \to D^{**}e\nu$ BF	0.4	1.1	0.5	0.1
$B \to D^{(\prime)}e\nu$ BF	0.2	0.9	0.2	0.0
Widths of $D^{(\prime)}$ states	0.2	0.5	0.2	0.0
J/ψ and $\psi(2S)$ background	0.1	0.2	0.1	0.1
τ background	0.2	0.7	0.3	0.1
B momentum	1.5	1.5	1.6	0.5
Bremsstrahlung	0.3	0.1	0.3	0.0
Final state radiation	0.6	0.6	0.5	0.6
Width of wide bin	0.4	0.4	0.3	0.0
$N_{B\bar{B}}$ normalization	1.1	1.1	1.1	1.1
Total exp. systematic uncertainty	$^{+4.2}_{-3.1}$	$^{+4.8}_{-3.7}$	$^{+4.7}_{-3.3}$	$^{+3.8}_{-3.0}$
Total exp. statistical uncertainty	3.8	5.0	3.5	2.8
Total exp. uncertainty	$^{+5.7}_{-4.9}$	$^{+7.0}_{-6.2}$	$^{+5.9}_{-4.8}$	$^{+4.7}_{-4.1}$

simulated events is measured in bins of the polar angle θ and laboratory momentum and used to correct the identification efficiency of electrons in $B\bar{B}$ events. The uncertainty of this correction is about 0.5%. The fit to the electron spectrum, in bins of 50 MeV/c, incorporates the uncertainty in the shape of the momentum distribution, and the momentum dependence of the electron efficiency and hadron misidentification using a covariance matrix to account for bin-to-bin correlations.

The requirement of at least four charged tracks in the event suppresses primarily QED processes in non-$B\bar{B}$ background, but also impacts both signal and other background events with low charged-particle multiplicity. To estimate the systematic uncertainty we increase the requirement on the minimum number of charged tracks in an event from four to five and observe changes in the partial BF of up to 1.9%. This estimation is rather conservative because the default requirement rejects less than 2% of reconstructed $B\bar{B}$ events.

To estimate the systematic uncertainty on the modeling of photons, the range of rejected photon energies was doubled. We increase the requirement on the minimum photon energy from the nominal value of 50 to 100 MeV and observe changes in the partial BF of up to 0.4% below 2.3 GeV/c, increasing at higher electron momenta.

The neural network is primarily designed to suppress non-$B\bar{B}$ backgrounds. Its input variables depend on the momenta of all tracks and the energies of all photons in the event. We have examined the sensitivity of the fit results to the requirement on the NN output value (default requirement at 0.0), and observe that for an increase to +0.15, the non-$B\bar{B}$ background decreases and the signal BF changes by up to −2.1%, whereas for a decrease to −0.15, the non-$B\bar{B}$ background increases and the signal BF changes by up to +3.6%. Decreasing the requirement on the NN output value increases the fraction of non-$B\bar{B}$ events, worsening the fit quality. Specifically, the fit probability changes from 20% for the default requirement to about 1% for a requirement at −0.15 and to about 10^{-7} for a requirement at −0.20. Increasing the requirement beyond +0.15 increases the statistical uncertainty by an amount consistent with the observed shifts in the branching ratio relative to the default value.

B. Signal electron spectrum

The momentum spectrum of the electrons from charmless semileptonic decays is not precisely known. It is composed of contributions from exclusive and inclusive decays.

Many of the exclusive decay modes are still unobserved or poorly measured due to small event samples, and the form factors for many of the observed exclusive decay modes are not measured, thus we have to rely on theoretical predictions. To estimate the sensitivity of the signal BF to the relative contributions of the different exclusive decay

modes, the BFs for $B \to \pi l\nu$, $B \to \rho l\nu$, $B \to \omega l\nu$, $B \to \eta l\nu$, $B \to \eta' l\nu$ and $B \to X_u^{\mathrm{nr}} l\nu$ are varied by 5%, 10%, 15%, 20%, 35% and 15% [2], respectively. The $B \to \pi l\nu$ and $B \to \rho l\nu$ form factors are varied between the ISGW2 model and current fits to measurements plus lattice QCD predictions. The observed impact of these variations on the fit result does not exceed 0.3%.

The systematic uncertainties inherent to the modeling of the inclusive lepton spectrum in charmless decays and their impact on the signal yield are studied by varying the SF parameters. For each set of SF parameters, we recalculate the signal momentum spectrum and repeat the fit to the data. Taking into account the uncertainties and correlations of the measured SF parameters, we derive the uncertainties. This is the largest source of systematic uncertainty for the measurement of the partial BFs and is discussed separately for each theoretical calculation in Sec. VIII.

C. Non-$B\bar{B}$ background

Systematic uncertainties associated with the subtraction of the non-$B\bar{B}$ background originate from the choice of the function describing the lepton momentum spectrum and the relative normalization of the on- and off-resonance data samples. We assess the impact of the fit function by replacing the default ansatz in Eq. (9) with the following:

$$f(\vec{a}, p) = (a_0 + a_1 p + a_2 p^2)$$
$$\times \exp(a_3 p + a_4 p^2 + a_5 p^3 + a_6 p^4 + a_7 p^5).$$
$$(11)$$

The observed difference is taken as the uncertainty, which is about 0.5% below 2.3 GeV/c and increases for higher momenta where this contribution dominates. The uncertainty in the relative normalization is taken as a constraint in the fit.

D. $B\bar{B}$ background

The momentum spectra of the dominant $B\bar{B}$ backgrounds are derived from MC simulations. Their relative contributions are adjusted in the fit.

The uncertainty in the lepton spectrum from the dominant decay modes was estimated by varying the form factors in $B \to D^* e\nu$ and $B \to D e\nu$ decays. The change in the partial BFs from these variations is less than 1.2%, and decreases for momenta above 2.3 GeV/c.

The sum of the BFs for the four decays to D^{**} resonances are included as a free parameter in the fit and the uncertainty is estimated by changing the relative BFs for decays to individual D^{**} resonances. The uncertainty due to the theoretical predictions of the form factors is estimated by varying the form factors for $B \to D_0^* e\nu$, $D_1' e\nu$, $D_1 e\nu$ and $D_2^* e\nu$. The impact on the fitted signal yield of each of these two sets of uncertainties in the $D^{**} e\nu$ spectrum is estimated

to be less than 0.6% over most of the spectrum, and decreases for momenta above 2.3 GeV/c.

Similarly, the impact of the uncertainties in the relative BFs of D' and D'^* resonances and their widths are evaluated. They change the fit results by less than 1% for momenta below 2.3 GeV/c, and are negligible above.

Electrons from $J/\psi \rightarrow e^+ e^-$ decays are one of the main sources of background near the endpoint, because unpaired $e^\pm$ from these decays are unaffected by the veto on the invariant mass of $e^+ e^-$ pairs. We observe a difference between the veto efficiency for electron pairs in data and simulation of (4.9 ± 0.9)% and also a difference in the observed momentum spectrum of the J/ψ. The $B\bar{B}$ MC simulation is corrected to match the measured spectrum and yield. To assess the impact of the veto efficiency, the number of J/ψ events is varied by 0.9%; this variation changes the signal BF by less than 0.2%. Background from $\psi(2S) \rightarrow e^+ e^-$ decays is significantly smaller, and its uncertainty is negligible.

Varying the relative BFs for semileptonic B decays involving $\tau^\pm$ leptons by 20% changes the fitted signal yield by up to 0.7%.

For background from hadronic B decays, the uncertainty in the spectrum is primarily due to the uncertainty in the momentum-dependent hadron misidentification. They have been studied and uncertainties in the normalization of π, K and p spectra are estimated to be 15%, 30% and 100%, respectively. Variations of the charged pion spectrum change the signal BFs by less than 0.8%, they are negligible for kaons and protons. The uncertainties in the momentum-dependent misidentification of pions, kaons and protons and antiprotons are included in the fit of the electron spectrum (uncertainty for shape of spectrum), taking into account bin-to-bin correlations.

E. B meson momentum spectrum

The B momentum is sensitive to the energies of the colliding beams which may vary slightly with time. Any variation in the momentum of the B meson in the $\Upsilon(4S)$ rest frame affects the shape of the electron spectrum near the endpoint. We have compared the simulated and measured momentum spectra for fully reconstructed hadronic decays of charged B mesons for different data taking periods. The widths of the total energy distributions agree well for all data, but for some of the data sets we observed a shift in the central value of up to 3.4 MeV relative to the simulation, which assumes a fixed c.m. energy. We correct the simulation for the observed shifts. The uncertainty of 0.1 MeV in this correction results in an estimated uncertainty on the signal BF of up to 1.6%.

F. Bremsstrahlung and radiative corrections

The MC simulations include the effects of bremsstrahlung and final state radiation. Corrections for QED radiation in the decay process are simulated using PHOTOS [18]. This simulation includes multiple-photon emission from the electron, but does not include electroweak corrections for quarks. The accuracy of this simulation has been compared to analytical calculations performed to $\mathcal{O}(\alpha)$ [18]. Based on this comparison we assign an uncertainty of 20% to the PHOTOS correction, leading to an uncertainty in the signal yield of about 0.6%.

The uncertainty in the energy loss of electrons due to bremsstrahlung in the beam pipe and tracking system is determined by the uncertainty in the thickness of the detector material, estimated to be $(0.0450 \pm 0.0014)X_0$ at normal incidence. The thickness of the material was verified using electrons from Bhabha scattering as a function of the polar angle relative to the beam. The impact of the uncertainty in the energy loss on the signal rate was estimated by calculating the impact of an additional $0.0014X_0$ of material. Relative shifts in the $B \rightarrow X_u e\nu$ BF due to variations of bremsstrahlung with respect to the default simulation are estimated to be about 0.3% up to 2.4 GeV/c and less at higher momenta.

G. Width of wide bin

The lower boundary of the large bin noticeably affects the fitted signal yield and uncertainty. For values less than 2.05 GeV/c, the uncertainty on the BF increases significantly, and for values greater than 2.1 GeV/c, the fit quality diminishes because the data and the predicted spectra differ at higher momenta. The impact of this sensitivity is estimated as the difference between the nominal fit with 2.1–2.7 GeV/c and a fit with a slightly lower boundary of the bin, 2.05–2.7 GeV/c. The relative change in the $B \rightarrow X_u e\nu$ BFs due to this variation is estimated to be 0.4% below 2 GeV/c and much lower at higher momenta.

VIII. RESULTS

The primary results of this study of the electron spectrum for inclusive semileptonic decays of B mesons are the total inclusive $B \rightarrow Xe\nu$ spectrum and BF, the extraction of the spectrum and partial and total BF for the charmless $B \rightarrow X_u e\nu$ decays and the determination of the CKM element $|V_{ub}|$, using four theoretical predictions based on different approaches to estimate the QCD corrections to the decay rate. All results are based on the full *BABAR* data sample and averaged over charged and neutral B mesons produced in $\Upsilon(4S)$ decays.

A. Total semileptonic spectrum and branching fraction

The differential BF for primary electrons in $B \rightarrow Xe\nu$ decays as a function of the electron momentum in the $\Upsilon(4S)$ rest frame is shown in Fig. 10. It is derived from the fit to the total observed electron spectrum for GGOU

calculations of the $B \rightarrow X_u e\nu$ spectrum. It is fully corrected for efficiencies and radiative effects. The data are normalized to the total number of produced B^+B^- and $B^0\bar{B}^0$ pairs, $N_{B\bar{B}} = (466.48 \pm 0.11_{\text{stat}} \pm 2.39_{\text{syst}}) \times 10^6$. The uncertainties shown represent the statistical uncertainties of the measurement, including the background subtraction and the uncertainties in the fit parameters. These uncertainties do not include systematic uncertainties, in particular those related to the prediction of the $B \rightarrow X_u e\nu$ spectrum. This spectrum and its uncertainties and the correlation matrix of the fit are available in the Supplemental Material [61].

The total inclusive semileptonic BF, averaged over charged and neutral B mesons, is obtained as the sum of the individual semileptonic BFs determined by the fit to the observed electron spectrum:

$$\mathcal{B}(B \rightarrow Xe\nu) = (10.34 \pm 0.04_{\text{stat}} \pm 0.26_{\text{syst}})\%. \quad (12)$$

Using GGOU for the predicted contribution from $B \rightarrow X_u e\nu$ decays, we obtain

$$\mathcal{B}(B \rightarrow X_c e\nu) = (10.18 \pm 0.03_{\text{stat}} \pm 0.24_{\text{syst}})\%, \quad (13)$$
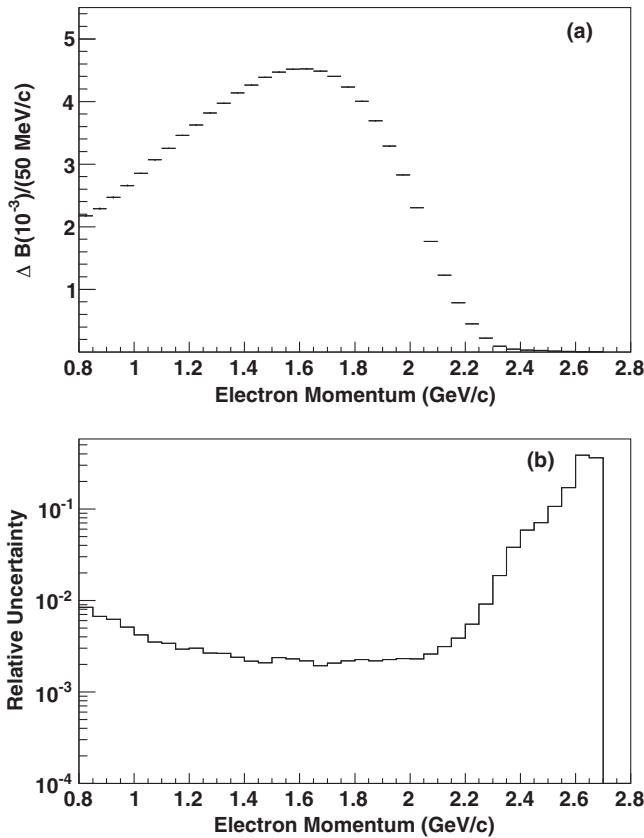
FIG. 10. Inclusive $B \rightarrow Xe\nu$ decays: (a) The differential branching fraction as a function of the electron momentum [in the $\Upsilon(4S)$ rest frame] after background subtraction and corrections for bremsstrahlung and final state radiation. (b) The relative statistical uncertainties on the background subtraction combined with the uncertainties of the fit parameters.
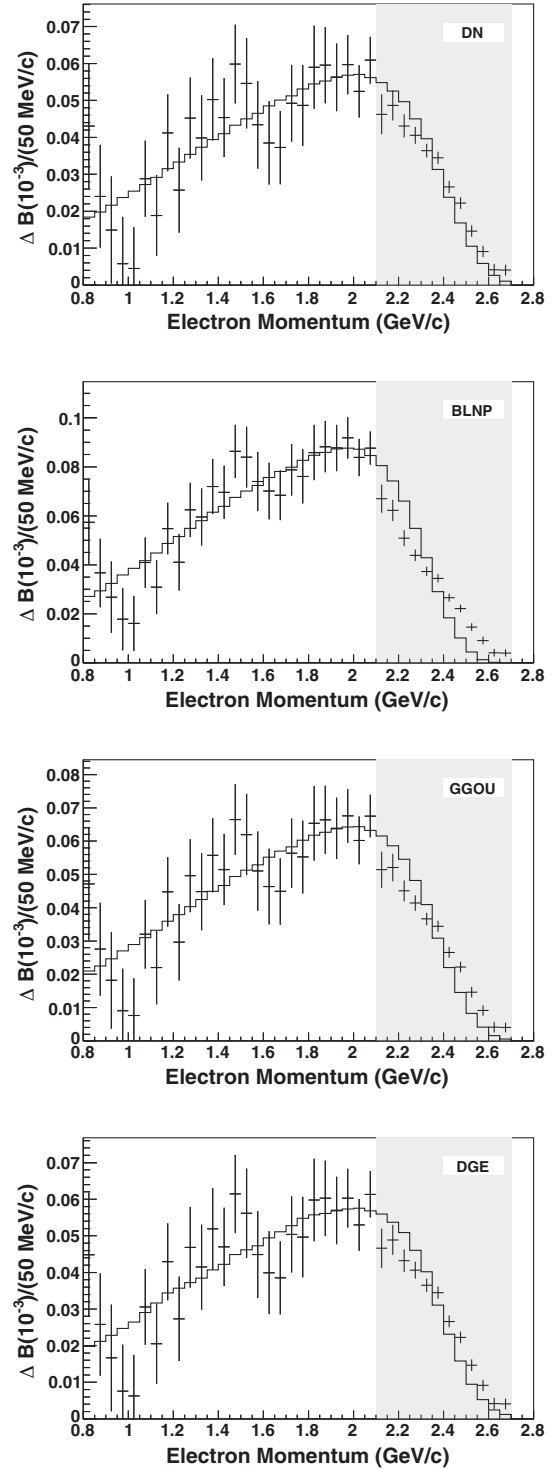
FIG. 11. The differential branching fraction for charmless semileptonic B decays (data points) as a function of the electron momentum [in the $\Upsilon(4S)$ rest frame] after background subtraction and corrections for bremsstrahlung and final state radiation, compared to the Monte Carlo simulation (histogram). The uncertainties indicate the statistical uncertainties on the background subtraction, including the uncertainties of the fit parameters. The shaded area indicates the momentum interval for which the on-resonance data are combined into a single bin.
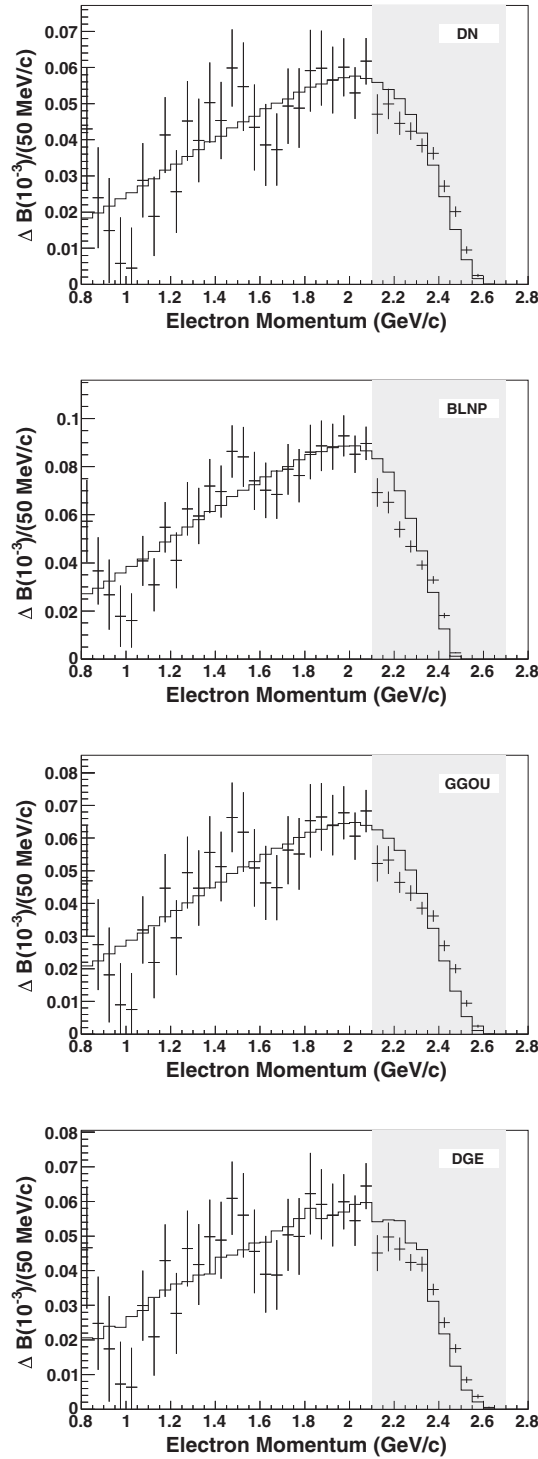
FIG. 12. The differential branching fraction for charmless semileptonic B decays (data points) as a function of the electron momentum (in the B rest frame) after background subtraction and corrections for bremsstrahlung and final state radiation, compared to the Monte Carlo simulation (histogram). The uncertainties indicate the statistical uncertainties on the background subtraction, including the uncertainties of the fit parameters. The shaded area indicates the momentum interval for which the on-resonance data are combined into a single bin.

where the stated systematic uncertainty takes into account the differences of about 1% between this result and those obtained with predictions of the $B \to X_u e\nu$ spectrum by DN, BLNP, and DGE. The results, which are dominated by systematic uncertainties, are consistent with the most recent HFAG average of $\mathcal{B}(B \to Xe\nu) = (10.86 \pm 0.16)\%$ and $\mathcal{B}(B \to X_c e\nu) = (10.65 \pm 0.16)\%$ [3].

B. Differential $B \to X_u e\nu$ branching fractions

The partial $B \to X_u e\nu$ BF for a given electron momentum interval Δp is determined as

$$\Delta\mathcal{B}(\Delta p) = \frac{N_{\text{tot}}(\Delta p) - N_{\text{bg}}(\Delta p)}{2\epsilon(\Delta p)N_{B\bar{B}}}(1 + \delta_{\text{rad}}(\Delta p)). \quad (14)$$

Here N_{tot} refers to the total number of selected electron candidates from the on-resonance data and N_{bg} refers to the total non-$B\bar{B}$ and $B\bar{B}$ background, as determined from the fit to the spectrum. $\epsilon(\Delta p)$ is the total efficiency for selecting a signal electron from $B \to X_u e\nu$ decays (including bremsstrahlung in the detector material), and δ_{rad} accounts for the impact of final state radiation on the electron spectrum. This momentum-dependent correction is derived from the MC simulation based on PHOTOS [18].

The differential BF for $B \to X_u e\nu$ decays, fully corrected for efficiencies and radiative effects, as a function of the electron momentum in the $\Upsilon(4S)$ rest frame is shown in Fig. 11, and in the B meson rest frame in Fig. 12. The error bars represent the statistical uncertainties of the measurement. They do not include the systematic uncertainties, nor the uncertainty due to the $B \to X_u e\nu$ predictions. For fits using the GGOU prediction for $B \to X_u e\nu$ the results for the differential BFs and the correlation matrix are available in the Supplemental Material [61]. Differences of the fitted
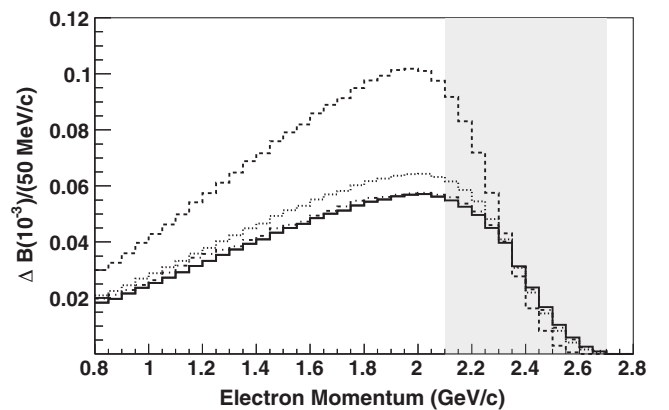

FIG. 13. The comparison of the theoretical differential branching fraction for charmless semileptonic B decays with normalization based on the fit as a function of the electron momentum [in the $\Upsilon(4S)$ rest frame] for DN (solid), BLNP (dashed), GGOU (dotted) and DGE (dash-dotted). The shaded area indicates the momentum interval for which the on-resonance data are combined into a single bin.
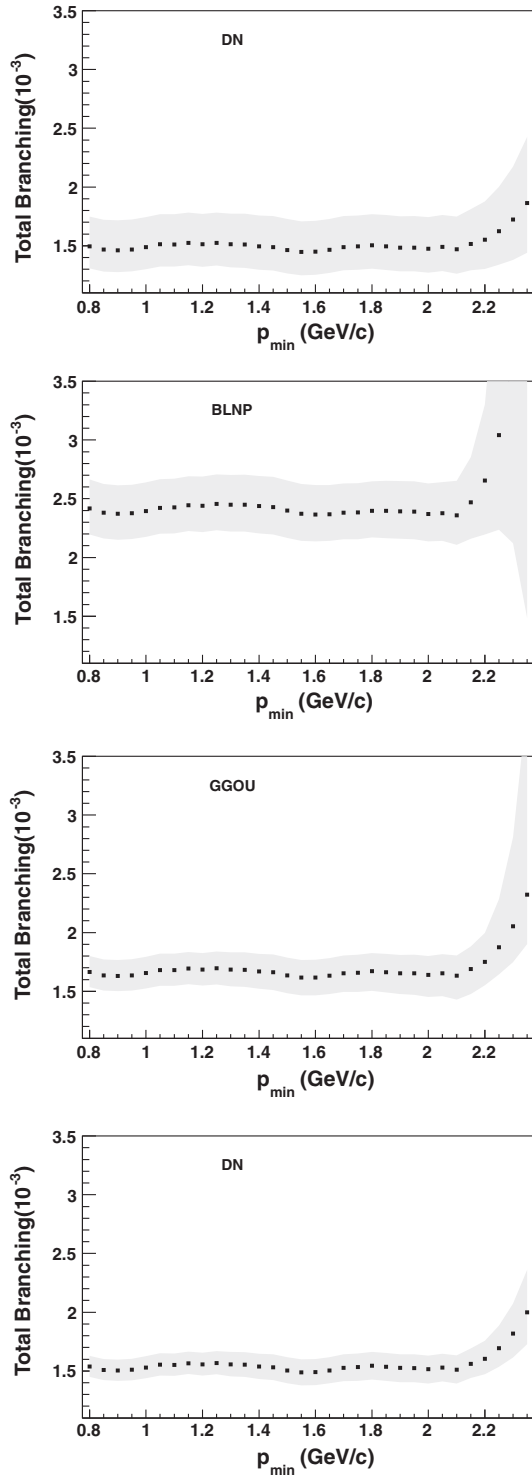
FIG. 14. Total branching fraction for $B \to X_u e\nu$ decays as a function $p_{\min}$, the lower limit of the electron momentum range used in the extraction of the signal and the total uncertainty which include experimental, SF parametrization and theoretical uncertainties, separately for DN, BLNP$_1$, GGOU$_1$, and DGE predictions of the decay rate used in the fit.
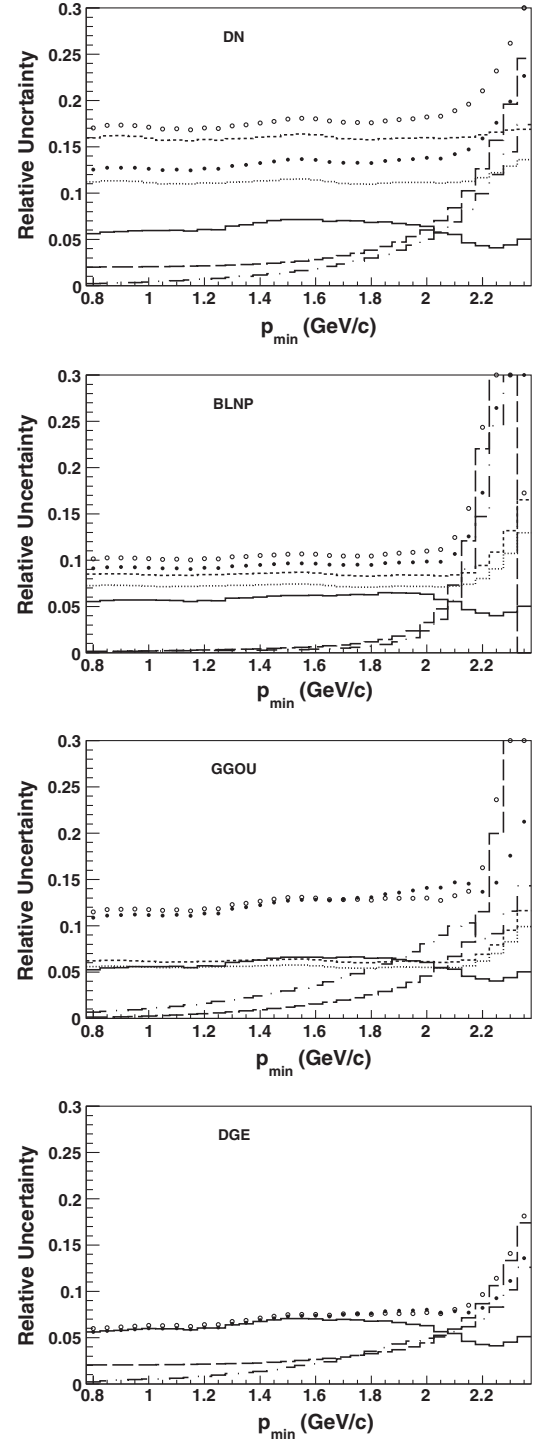
FIG. 15. Relative uncertainties on the signal BF for DN, BLNP$_1$, GGOU$_1$, and DGE calculations as a function of $p_{\min}$, the lower limit of the electron momentum range used in the signal extraction, open and solid circles: total uncertainties (positive and negative uncertainties), solid line: experimental, long-dashed and long-dash-dotted lines: theoretical, dashed and dotted lines: SF uncertainty.

spectra and the data are clearly visible inside the wide bin, and are most pronounced for BLNP, for which the predicted rate is negative above 2.4 GeV/c. In all cases the data exceed the predictions above 2.3 GeV/c, and are lower
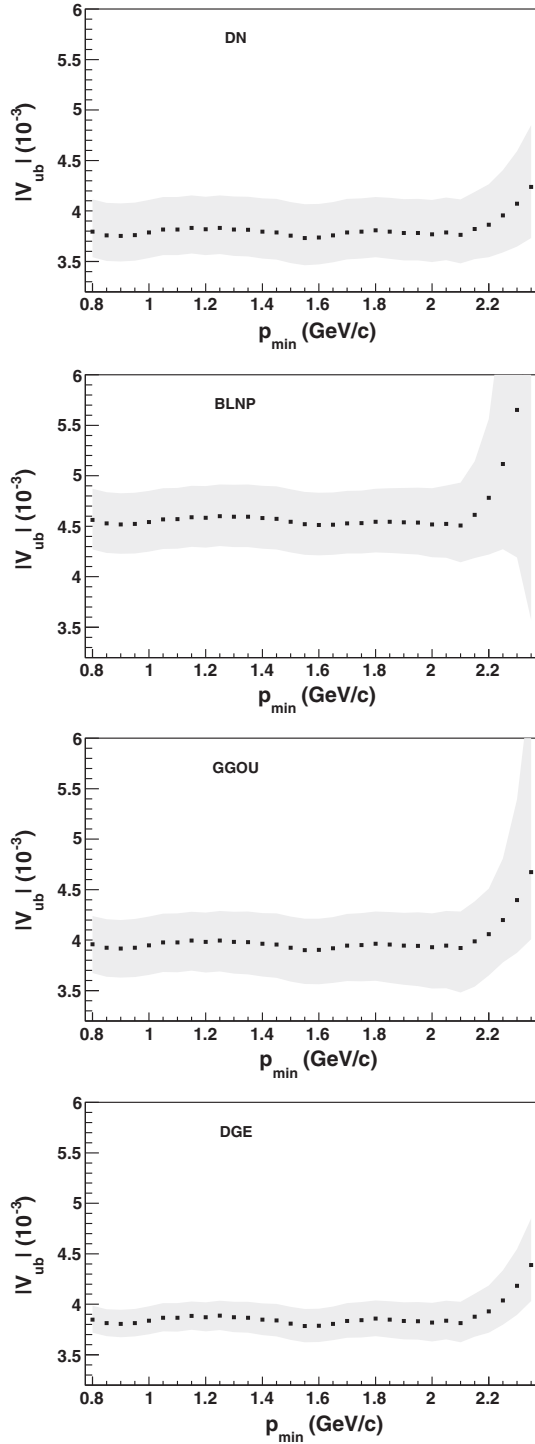
FIG. 16. $|V_{ub}|$ as a function of $p_{\min}$, the lower limit of the momentum range used in the extraction of the signal, for DN, BLNP$_1$, GGOU$_1$, and DGE predictions of the decay rate.
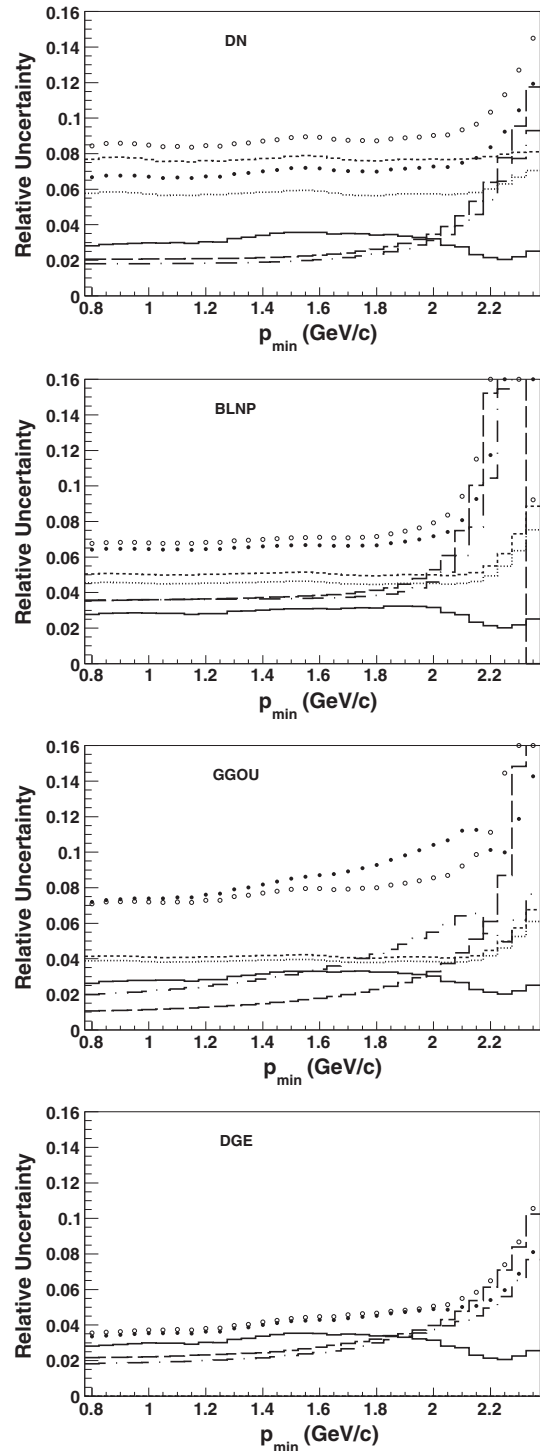
FIG. 17.   Relative uncertainties on $|V_{ub}|$ for four different predictions as a function of the lower limit $p_{\min}$ of the momentum range used to extract the signal, for DN, BLNP$_1$, GGOU$_1$, and DGE predictions of the signal rate: total uncertainties (open and solid dots for positive and negative uncertainties), experimental (solid histogram), SF parametrization (dashed and dotted histograms for positive and negative uncertainties), and theoretical (long-dashed and long-dotted histograms for positive and negative uncertainties).

below, such that the data summed over the wide bin agree with the predictions in this momentum range.

A comparison of the predicted $B \to X_u e\nu$ electron spectra, each normalized to the fitted rate is presented in Fig. 13. While these spectra agree reasonably well for DN, GGOU and DGE, the BLNP prediction deviates substantially. This is explained by a lower predicted rate for momenta above 2.1 GeV/c, which leads to a significantly larger fitted normalization of this spectrum.

C. Total charmless branching fraction

The total BF for charmless $B \to X_u e\nu$ decays is determined from the partial BF $\Delta\mathcal{B}(\Delta p)$ in a given momentum range Δp, as follows:

$$\mathcal{B}(B \to X_u e\nu) = \Delta\mathcal{B}(\Delta p)/f_u(\Delta p), \qquad (15)$$

where $f_u(\Delta p)$ is the theoretically predicted fraction of the electron spectrum. These total BF which have been determined as a function of $p_{\min}$, the lower limit of the momentum range $\Delta p = [p_{\min}, 2.7 \text{ GeV}/c]$, (with fixed upper limit of 2.7 GeV/c) and their relative uncertainties are shown in Figs. 14 and 15, for the four different theoretical predictions. Up to 2.1 GeV/c, the resulting BFs are independent of $p_{\min}$, above 2.1 GeV/c, the BFs and their uncertainties increase significantly.

D. Extraction of $|V_{ub}|$

We rely on four different theoretical calculations to extract $|V_{ub}|$ from the inclusive electron spectrum for $B \to X_u e\nu$ decays. The $|V_{ub}|$ and relative uncertainties

are shown in Figs. 16 and 17, respectively. The experimental uncertainty includes statistical uncertainty and the uncertainty of the background subtraction. The SF uncertainty includes stated uncertainties on the SF parameters and their correlation. Specifically, we adopt the maximum deviation of the central value of $|V_{ub}|$ from selected SF parameter values on the error ellipse. The resulting values of $|V_{ub}|$ and their uncertainties are largely constant for lower values of $p_{\min}$, and rise sharply above 2.1 GeV/c.

E. Summary of results

The results for $\mathcal{B}(B \to X_u e\nu)$ and $|V_{ub}|$ are presented for the wide momentum range, $p_e = 0.8$–2.7 GeV/c, in Table VI, and for the narrower range, $p_e = 2.1$–2.7 GeV/c, in Table VII. In these tables, the first uncertainty represents the combined statistical and systematic experimental uncertainties of the partial BF measurement, the second refers to the uncertainty in the determination of the shape function parameters used by the DN, BLNP, and GGOU, and the third is due to the uncertainties of the QCD calculations.

For GGOU, we present results for two sets of SF parameters in the kinetic scheme, one based on fits to moments of lepton energy and hadron mass distributions from $B \to X_c \ell\nu$ decays and further constrained by the c-quark mass (GGOU$_1$), the other based on including the moments of the photon spectrum in $B \to X_s \gamma$ decays (GGOU$_2$).

For BLNP, we present results for four sets of SF parameters in the SF scheme, based on fits of the moments of the lepton energy and hadron mass distributions in

TABLE VI. Results for $\Delta\mathcal{B}(B \to X_u e\nu)$, $\mathcal{B}(B \to X_u e\nu)$, $|V_{ub}|$ and $\Delta\zeta(\Delta p)$ based on the electron momentum range $\Delta p = 0.8$–2.7 GeV/c for different theoretical predictions, with experimental, SF, and theory uncertainties.

$\Delta\mathcal{B}[10^{-3}]$	$\mathcal{B}[10^{-3}]$	$|V_{ub}|[10^{-3}]$	$\Delta\zeta(\Delta p)[\text{ps}^{-1}]$
	DN		
$1.397 \pm 0.078_{\text{exp}}\,{}^{+0.214}_{-0.153}\,{}_{\text{SF}}$	$1.494 \pm 0.084_{\text{exp}}\,{}^{+0.239}_{-0.167}\,{}_{\text{SF}}\,{}^{+0.030}_{-0.003}\,{}_{\text{theory}}$	$3.794 \pm 0.107_{\text{exp}}\,{}^{+0.292}_{-0.219}\,{}_{\text{SF}}\,{}^{+0.078}_{-0.068}\,{}_{\text{theory}}$	$61.43\,{}^{+0.20}_{-0.33}\,{}_{\text{SF}}\,{}^{+2.28}_{-2.45}\,{}_{\text{theory}}$
	DGE		
$1.433 \pm 0.081_{\text{exp}}$	$1.537 \pm 0.086_{\text{exp}}\,{}^{+0.031}_{-0.003}\,{}_{\text{theory}}$	$3.848 \pm 0.108_{\text{exp}}\,{}^{+0.084}_{-0.070}\,{}_{\text{theory}}$	$61.26\,{}^{+2.30}_{-2.58}\,{}_{\text{theory}}$
	$X_c\ell\nu$, m_c constraint fit of SF parameters, GGOU$_1$		
$1.554 \pm 0.082_{\text{exp}}\,{}^{+0.095}_{-0.086}\,{}_{\text{SF}}$	$1.665 \pm 0.087_{\text{exp}}\,{}^{+0.103}_{-0.093}\,{}_{\text{SF}}\,{}^{+0.002}_{-0.011}\,{}_{\text{theory}}$	$3.959 \pm 0.104_{\text{exp}}\,{}^{-0.154}_{+0.164}\,{}_{\text{SF}}\,{}^{-0.079}_{+0.042}\,{}_{\text{theory}}$	$62.76\,{}^{+1.59}_{-1.55}\,{}_{\text{SF}}\,{}^{-1.32}_{+2.58}\,{}_{\text{theory}}$
	$X_c\ell\nu$, $X_s\gamma$ constraint fit of SF parameters, GGOU$_2$		
$1.551 \pm 0.081_{\text{exp}}\,{}^{-0.100}_{+0.117}\,{}_{\text{SF}}$	$1.661 \pm 0.086_{\text{exp}}\,{}^{-0.109}_{+0.127}\,{}_{\text{SF}}\,{}^{-0.011}_{+0.008}\,{}_{\text{theory}}$	$3.936 \pm 0.102_{\text{exp}}\,{}^{-0.188}_{+0.202}\,{}_{\text{SF}}\,{}^{-0.086}_{+0.168}\,{}_{\text{theory}}$	$63.38\,{}^{+2.15}_{-2.15}\,{}_{\text{SF}}\,{}^{-5.08}_{+2.87}\,{}_{\text{theory}}$
	$X_c\ell\nu$, m_c constraint fit of SF parameters with $\mu_i = 2.0$ GeV, BLNP$_1$		
$2.268 \pm 0.125_{\text{exp}}\,{}^{-0.163}_{+0.191}\,{}_{\text{SF}}$	$2.418 \pm 0.134_{\text{exp}}\,{}^{-0.176}_{+0.205}\,{}_{\text{SF}}\,{}^{-0.003}_{+0.003}\,{}_{\text{theory}}$	$4.563 \pm 0.126_{\text{exp}}\,{}^{-0.208}_{+0.230}\,{}_{\text{SF}}\,{}^{-0.163}_{+0.162}\,{}_{\text{theory}}$	$68.93\,{}^{+1.88}_{-1.85}\,{}_{\text{SF}}\,{}^{-4.65}_{+5.20}\,{}_{\text{theory}}$
	$X_c\ell\nu$, m_c constraint fit of SF parameters with $\mu_i = 1.5$ GeV, BLNP$_2$		
$2.924 \pm 0.112_{\text{exp}}\,{}^{-0.137}_{+0.152}\,{}_{\text{SF}}$	$2.160 \pm 0.120_{\text{exp}}\,{}^{-0.148}_{+0.164}\,{}_{\text{SF}}\,{}^{-0.003}_{+0.002}\,{}_{\text{theory}}$	$4.406 \pm 0.122_{\text{exp}}\,{}^{-0.193}_{+0.203}\,{}_{\text{SF}}\,{}^{-0.189}_{+0.176}\,{}_{\text{theory}}$	$66.00\,{}^{+1.88}_{-1.82}\,{}_{\text{SF}}\,{}^{-4.96}_{+6.06}\,{}_{\text{theory}}$
	$X_c\ell\nu$, $X_s\gamma$ constraint fit of SF parameters with $\mu_i = 2.0$ GeV, BLNP$_3$		
$2.157 \pm 0.120_{\text{exp}}\,{}^{-0.176}_{+0.207}\,{}_{\text{SF}}$	$2.298 \pm 0.128_{\text{exp}}\,{}^{-0.189}_{+0.222}\,{}_{\text{SF}}\,{}^{-0.003}_{+0.003}\,{}_{\text{theory}}$	$4.420 \pm 0.123_{\text{exp}}\,{}^{-0.251}_{+0.273}\,{}_{\text{SF}}\,{}^{-0.158}_{+0.156}\,{}_{\text{theory}}$	$66.94\,{}^{+2.69}_{-2.62}\,{}_{\text{SF}}\,{}^{-5.02}_{+6.15}\,{}_{\text{theory}}$
	$X_c\ell\nu$, $X_s\gamma$ constraint fit of SF parameters with $\mu_i = 1.5$ GeV, BLNP$_4$		
$1.931 \pm 0.108_{\text{exp}}\,{}^{-0.147}_{+0.172}\,{}_{\text{SF}}$	$2.059 \pm 0.115_{\text{exp}}\,{}^{-0.158}_{+0.185}\,{}_{\text{SF}}\,{}^{-0.002}_{+0.002}\,{}_{\text{theory}}$	$4.273 \pm 0.119_{\text{exp}}\,{}^{-0.243}_{+0.263}\,{}_{\text{SF}}\,{}^{-0.184}_{+0.170}\,{}_{\text{theory}}$	$69.88\,{}^{+2.70}_{-2.64}\,{}_{\text{SF}}\,{}^{-4.69}_{+5.26}\,{}_{\text{theory}}$

TABLE VII.   Results for $\Delta\mathcal{B}(B \to X_u e\nu)$, $\mathcal{B}(B \to X_u e\nu)$, $|V_{ub}|$ and $\Delta\zeta(\Delta p)$ based on the electron momentum range $\Delta p = 2.1$–2.7 GeV/c for different theoretical predictions, with experimental, SF, and theory uncertainties.

$\Delta\mathcal{B}[10^{-3}]$	$\mathcal{B}[10^{-3}]$	$|V_{ub}|[10^{-3}]$	$\Delta\zeta(\Delta p)[\text{ps}^{-1}]$
	DN		
$0.330 \pm 0.018_{\text{exp}}{}^{-0.009}_{+0.009}{}_{\text{SF}}$	$1.471 \pm 0.081_{\text{exp}}{}^{-0.164}_{+0.235}{}_{\text{SF}}{}^{-0.101}_{+0.124}{}_{\text{theory}}$	$3.764 \pm 0.104_{\text{exp}}{}^{-0.216}_{+0.290}{}_{\text{SF}}{}^{-0.148}_{+0.170}{}_{\text{theory}}$	$14.75^{+1.41}_{-1.70}{}_{\text{SF}}{}^{-1.24}_{+1.23}{}_{\text{theory}}$
	DGE		
$0.331 \pm 0.018_{\text{exp}}$	$1.511 \pm 0.082_{\text{exp}}{}^{-0.085}_{+0.090}{}_{\text{theory}}$	$3.815 \pm 0.104_{\text{exp}}{}^{-0.160}_{+0.182}{}_{\text{theory}}$	$14.40^{+1.29}_{-1.28}{}_{\text{theory}}$
	$X_c\ell\nu$, m_c constraint fit of SF parameters, GGOU$_1$		
$0.342 \pm 0.018_{\text{exp}}{}^{-0.006}_{+0.007}{}_{\text{SF}}$	$1.634 \pm 0.087_{\text{exp}}{}^{-0.090}_{+0.100}{}_{\text{SF}}{}^{-0.163}_{+0.109}{}_{\text{theory}}$	$3.922 \pm 0.104_{\text{exp}}{}^{-0.150}_{+0.160}{}_{\text{SF}}{}^{-0.251}_{+0.170}{}_{\text{theory}}$	$14.06^{+0.87}_{-0.82}{}_{\text{SF}}{}^{-1.14}_{+1.99}{}_{\text{theory}}$
	$X_c\ell\nu$, $X_s\gamma$ constraint fit of SF parameters, GGOU$_2$		
$0.342 \pm 0.018_{\text{exp}}{}^{-0.007}_{+0.008}{}_{\text{SF}}$	$1.630 \pm 0.086_{\text{exp}}{}^{-0.105}_{+0.122}{}_{\text{SF}}{}^{-0.189}_{+0.188}{}_{\text{theory}}$	$3.899 \pm 0.103_{\text{exp}}{}^{-0.185}_{+0.198}{}_{\text{SF}}{}^{-0.289}_{+0.381}{}_{\text{theory}}$	$14.23^{+1.12}_{-1.08}{}_{\text{SF}}{}^{-2.42}_{+2.37}{}_{\text{theory}}$
	$X_c\ell\nu$, m_c constraint fit of SF parameters with $\mu_i = 2.0$ GeV, BLNP$_1$		
$0.397 \pm 0.022_{\text{exp}}{}^{-0.012}_{+0.014}{}_{\text{SF}}$	$2.359 \pm 0.130_{\text{exp}}{}^{-0.170}_{+0.199}{}_{\text{SF}}{}^{-0.133}_{+0.173}{}_{\text{theory}}$	$4.507 \pm 0.124_{\text{exp}}{}^{-0.204}_{+0.226}{}_{\text{SF}}{}^{-0.275}_{+0.337}{}_{\text{theory}}$	$12.36^{+0.89}_{-0.83}{}_{\text{SF}}{}^{-1.66}_{+1.66}{}_{\text{theory}}$
	$X_c\ell\nu$, m_c constraint fit of SF parameters with $\mu_i = 1.5$ GeV, BLNP$_2$		
$0.376 \pm 0.021_{\text{exp}}{}^{-0.010}_{+0.011}{}_{\text{SF}}$	$2.110 \pm 0.117_{\text{exp}}{}^{-0.143}_{+0.158}{}_{\text{SF}}{}^{-0.087}_{+0.128}{}_{\text{theory}}$	$4.356 \pm 0.120_{\text{exp}}{}^{-0.190}_{+0.198}{}_{\text{SF}}{}^{-0.265}_{+0.317}{}_{\text{theory}}$	$12.55^{+0.92}_{-0.85}{}_{\text{SF}}{}^{-1.64}_{+1.68}{}_{\text{theory}}$
	$X_c\ell\nu$, $X_s\gamma$ constraint fit of SF parameters with $\mu_i = 2.0$ GeV, BLNP$_3$		
$0.389 \pm 0.022_{\text{exp}}{}^{-0.013}_{+0.015}{}_{\text{SF}}$	$2.244 \pm 0.124_{\text{exp}}{}^{-0.183}_{+0.215}{}_{\text{SF}}{}^{-0.117}_{+0.152}{}_{\text{theory}}$	$4.367 \pm 0.121_{\text{exp}}{}^{-0.248}_{+0.270}{}_{\text{SF}}{}^{-0.257}_{+0.313}{}_{\text{theory}}$	$12.91^{+1.25}_{-1.17}{}_{\text{SF}}{}^{-1.67}_{+1.67}{}_{\text{theory}}$
	$X_c\ell\nu$, $X_s\gamma$ constraint fit of SF parameters with $\mu_i = 1.5$ GeV, BLNP$_4$		
$0.370 \pm 0.020_{\text{exp}}{}^{-0.010}_{+0.012}{}_{\text{SF}}$	$2.013 \pm 0.111_{\text{exp}}{}^{-0.153}_{+0.179}{}_{\text{SF}}{}^{-0.075}_{+0.112}{}_{\text{theory}}$	$4.225 \pm 0.116_{\text{exp}}{}^{-0.239}_{+0.259}{}_{\text{SF}}{}^{-0.250}_{+0.296}{}_{\text{theory}}$	$13.10^{+1.30}_{-1.20}{}_{\text{SF}}{}^{-1.66}_{+1.70}{}_{\text{theory}}$

$B \to X_c\ell\nu$ decays: two with a constraint on the charm quark mass (BLNP$_1$, BLNP$_2$), and the other two on including the moments of the photon spectrum in $B \to X_s\gamma$ decays (BLNP$_3$, BLNP$_4$). For each pair of results, we choose two values for the scale parameter, $\mu_i = 2.0$ GeV and $\mu_i = 1.5$ GeV. The results with the smaller scale parameter have the lower SF uncertainties.

The resulting total BFs and $|V_{ub}|$ for DN, GGOU and DGE agree well within their uncertainties, while the BF results for BLNP are between about 25% and 60%, and the values of $|V_{ub}|$ are about 8%–20% higher than for the other three QCD calculations. The BFs and the values of $|V_{ub}|$ that are extracted for the momentum range with $p_{\min} = 0.8$ GeV/c exceed those for $p_{\min} = 2.1$ GeV/c on average by ∼2% and ∼1%, respectively.

TABLE VIII.   Simple ansatz describing the dependence of the total branching fraction $\mathcal{B}(B \to X_u e\nu)$ and $|V_{ub}|$ on the shape function parameters x_1 and x_2, i.e., $\bar{\Lambda}^{\text{SF}}$ and λ_1^{SF} for DN, and m$_b$ and μ_π^2 for BLNP and GGOU.

$\mathcal{B} \times 10^3$ QCD prediction	x_1^0	x_2^0	c_0	c_1	c_2
DN	0.49	−0.24	1.494	+1.498	−0.072
BLNP$_{1,3}$	4.561	0.149	2.418	−34.608	−0.252
GGOU$_{1,2}$	4.560	0.453	1.665	−13.714	−0.314

$|V_{ub}| \times 10^3$ QCD prediction	x_1^0	x_2^0	c_0	c_1	c_2
DN	0.49	−0.24	3.794	+1.949	−0.109
BLNP$_{1,3}$	4.561	0.149	4.563	−43.621	−0.178
GGOU$_{1,2}$	4.560	0.453	3.959	−25.024	−0.357

To quantify the dependence of the total BF (and also $|V_{ub}|$) on the SF parameters we have introduced a simple relation,

$$\mathcal{B} \times 10^3 = c_0 + c_1 \times \frac{x_1 - x_1^0}{x_1^0} + c_2 \times \frac{x_2 - x_2^0}{x_2^0}. \quad (16)$$

The parameters c_i and the default SF parameters values x_i^0 are given in Table VIII.

IX. CONCLUSIONS

Based on the total *BABAR* data sample, we have measured the inclusive electron spectrum and BF, averaged over $B^\pm$ and B^0 mesons, $\mathcal{B}(B \to Xe\nu) = (10.34 \pm 0.04_{\text{stat}} \pm 0.26_{\text{syst}})\%$. From a fit to this observed inclusive spectrum, we have extracted the spectrum and partial BFs for the CKM suppressed $B \to X_u e\nu$ decays in the momentum range $0.8 < p_e < 2.7$ GeV/c. This fit requires as input knowledge of the shapes of the signal and all background contributions, many of them derived from measurements. The most challenging input is the prediction of the shape of the $B \to X_u e\nu$ spectrum, for which we rely on predictions of four sets of QCD calculations that involve estimates of the perturbative and nonperturbative hadronic corrections. Specifically, we have used the earlier calculations by De Fazio and Neubert [19] and Kagan and Neubert [37], and the more comprehensive approaches by Lange, Neubert and Paz [43], Gambino, Giordano, Ossola and Uraltsev [45,46], and Andersen and Gardi [47,48,50]. These calculations also enter the determination of $|V_{ub}|$. The resulting values of
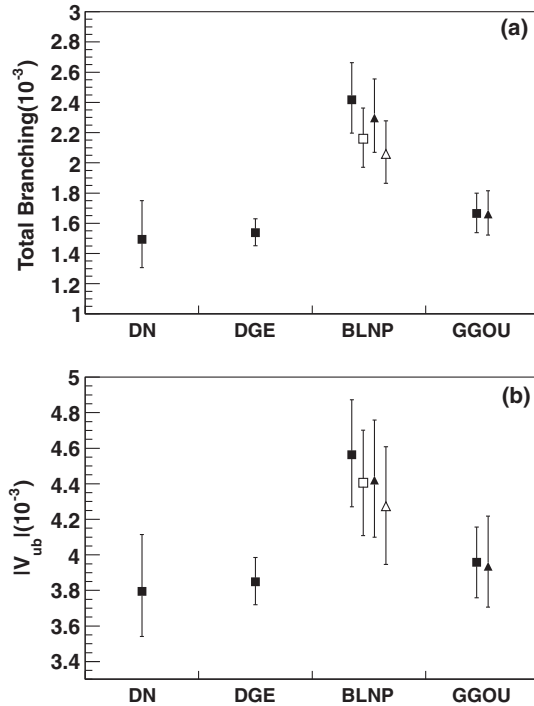
FIG. 18. Results for (a) $\mathcal{B}(B \to X_u e\nu)$, and (b) $|V_{ub}|$ based on the momentum range $p_e = 0.8$–2.7 GeV/c for different QCD calculations and SF parametrizations (Table VI). For BLNP and GGOU: solid squares—$X_c \ell \nu$ moment fits with m_c constraint (BLNP$_1$ and GGOU$_1$), solid triangles—$X_c \ell \nu$ and $X_s \gamma$ moment fits (BLNP$_3$ and GGOU$_2$), open squares or triangles—the same constraints for translation of SF parameters from "kinetic" to "shape-function" scheme with $\mu_i = 1.5$ GeV (BLNP$_2$ and BLNP$_4$).

$|V_{ub}|$ and the total uncertainties are shown in Fig. 18. The measurements based on DN, DGE, and GGOU agree well within their uncertainties, while the BLNP calculations result in significantly higher values for both the total BF and $|V_{ub}|$. The differences of measured $|V_{ub}|$ values and the world averages [3] are 0.3σ (BLNP), 1.9σ (GGOU), 2.5σ (DGE).

These results are in very good agreement with the earlier *BABAR* measurements [8] of the inclusive lepton spectrum at the $\Upsilon(4S)$ resonance, which showed similar differences between results based on the DN and BLNP predictions.

As in earlier measurements based on the lepton momentum spectrum, the uncertainties on the $B \to X_u e\nu$ lepton spectrum and the extraction of $|V_{ub}|$ are dominated by the current knowledge of the shapes of signal and background spectra, in particular in the theoretical predictions of the spectrum, both in terms of perturbative and nonperturbative corrections to the predicted rate.

[1] M. Kobayashi and T. Maskawa, Prog. Theor. Phys. **49**, 652 (1973).

[2] K. A. Olive *et al.* (Particle Data Group), Chin. Phys. C **38**, 090001 (2014).

[3] Y. Amhis *et al.* (Heavy Flavor Averaging Group), arXiv:1412.7515.

[4] M. Shifman and M. Voloshin, Sov. J. Nucl. Phys. **41**, 120 (1985); J. Chay, H. Georgi, and B. Grinstein, Phys. Lett. B **247**, 399 (1990); I. I. Bigi and N. Uraltsev, Phys. Lett. B **280**, 271 (1992); A. V. Manohar and M. B. Wise, Phys. Rev. D **49**, 1310 (1994); B. Blok, L. Koyrakh, M. Shifman, and A. I. Vainshtein, Phys. Rev. D **49**, 3356 (1994).

[5] H. Albrecht *et al.* (ARGUS Collaboration), Phys. Lett. B **234**, 409 (1990); **255**, 297 (1991).

[6] R. Fulton *et al.* (CLEO Collaboration), Phys. Rev. Lett. **64**, 16 (1990); J. Bartelt *et al.*, Phys. Rev. Lett. **71**, 4111 (1993).

[7] A. Bornheim *et al.* (CLEO Collaboration), Phys. Rev. Lett. **88**, 231803 (2002).

[8] B. Aubert *et al.* (*BABAR* Collaboration), Phys. Rev. D **73**, 012006 (2006).

[9] A. Limosani *et al.* (Belle Collaboration), Phys. Lett. B **621**, 28 (2005).

[10] M. Acciarri *et al.* (L3 Collaboration), Phys. Lett. B **436**, 174 (1998).

[11] R. Barate *et al.* (ALEPH Collaboration), Eur. Phys. J. C **6**, 555 (1999).

[12] P. Abreu *et al.* (DELPHI Collaboration), Phys. Lett. B **478**, 14 (2000).

[13] G. Abbiendi *et al.* (OPAL Collaboration), Eur. Phys. J. C **21**, 399 (2001).

[14] R. Aaij *et al.* (LHCb Collaboration), Nat. Phys. **11**, 743 (2015).

[15] B. Aubert *et al.* (*BABAR* Collaboration), Nucl. Instrum. Methods Phys. Res., Sect. A **479**, 1 (2002); **729**, 615 (2013).

[16] J. P. Lees *et al.* (*BABAR* Collaboration), Nucl. Instrum. Methods Phys. Res., Sect. A **726**, 203 (2013).

[17] S. Agostinelli *et al.* (GEANT4 Collaboration), Nucl. Instrum. Methods Phys. Res., Sect. A **506**, 250 (2003).

[18] E. Richter-Was, Phys. Lett. B **303**, 163 (1993).

[19] F. De Fazio and M. Neubert, J. High Energy Phys. 06 (1999) 017.

[20] N. Isgur, D. Scora, B. Grinstein, and M. B. Wise, Phys. Rev. D **39**, 799 (1989); D. Scora and N. Isgur, Phys. Rev. D **52**, 2783 (1995).

[21] T. Sjöstrand, Comput. Phys. Commun. **82**, 74 (1994).

[22] I. I. Bigi, M. Shifman, and N. G. Uraltsev, Annu. Rev. Nucl. Part. Sci. **47**, 591 (1997).

[23] I. Caprini, L. Lellouch, and M. Neubert, Nucl. Phys. **B530**, 153 (1998).

[24] B. Grinstein and Z. Ligeti, Phys. Lett. B **526**, 345 (2002).

[25] A. K. Leibovich, Z. Ligeti, I. W. Stewart, and M. B. Wise, Phys. Rev. D **57**, 308 (1998).

[26] J. L. Goity and W. Roberts, Phys. Rev. D **51**, 3459 (1995).

[27] F. U. Bernlocher, Z. Ligeti, and S. Turczyk, Phys. Rev. D **85**, 094033 (2012).

[28] J. P. Lees *et al.* (*BABAR* Collaboration), Phys. Rev. Lett. **116**, 041801 (2016).

[29] P. del Amo Sanchez *et al.*, Phys. Rev. D **82**, 111101 (2010).

[30] R. Aaij *et al.* (LHCb Collaboration), J. High Energy Phys. 09 (2013) 145.

[31] Kazuo Abe *et al.* (Belle Collaboration), Phys. Rev. Lett. **94**, 221805 (2005).

[32] R. Aaij *et al.* (LHCb Collaboration), Phys. Rev. D **84**, 092001 (2011); **85**, 039904(E) (2012).

[33] B. Aubert *et al.* (*BABAR* Collaboration), Phys. Rev. D **75**, 072002 (2007).

[34] M. Neubert, Phys. Rev. D **49**, 3392 (1994); C. W. Bauer and A. V. Manohar, Phys. Rev. D **70**, 034024 (2004).

[35] I. I. Bigi, M. A. Shifman, N. G. Uraltsev, and A. I. Vainshtein, Int. J. Mod. Phys. A **09**, 2467 (1994).

[36] M. Neubert, Phys. Rev. D **49**, 4623 (1994).

[37] A. L. Kagan and M. Neubert, Eur. Phys. J. C **7**, 5 (1999).

[38] S. W. Bosch, B. O. Lange, M. Neubert, and G. Paz, Nucl. Phys. **B699**, 335 (2004).

[39] M. Neubert, Eur. Phys. J. C **40**, 165 (2005).

[40] S. W. Bosch, M. Neubert, and G. Paz, J. High Energy Phys. 11 (2004) 073.

[41] M. Neubert, arXiv:hep-ph/0411027.

[42] M. Neubert, Phys. Lett. B **612**, 13 (2005); (private communication).

[43] B. Lange, M. Neubert, and G. Paz, arXiv:hep-ph/0504071.

[44] C. Greub, M. Neubert, and B. D. Pecjak, Eur. Phys. J. C **65**, 501 (2010).

[45] P. Gambino, P. Giordano, G. Ossola, and N. Uraltsev, J. High Energy Phys. 10 (2007) 058.

[46] P. Gambino, J. High Energy Phys. 09 (2011) 055.

[47] E. Gardi, arXiv:hep-ph/0606080.

[48] J. R. Andersen and E. Gardi, J. High Energy Phys. 01 (2006) 097.

[49] J. R. Andersen and E. Gardi, J. High Energy Phys. 01 (2007) 029.

[50] E. Gardi, arXiv:0806.4524.

[51] N. Uraltsev, Int. J. Mod. Phys. A **14**, 4641 (1999); (private communication).

[52] B. Aubert *et al.* (*BABAR* Collaboration), Phys. Rev. D **72**, 052004 (2005).

[53] N. Uraltsev, Int. J. Mod. Phys. A **11**, 515 (1996).

[54] I. Bigi, M. Shifman, and N. Uraltsev, Annu. Rev. Nucl. Part. Sci. **47**, 591 (1997).

[55] I. I. Bigi, arXiv:hep-ph/9907270.

[56] A. H. Hoang, Z. Ligeti, and A. V. Manohar, Phys. Rev. Lett. **82**, 277 (1999).

[57] A. H. Hoang, Z. Ligeti, and A. V. Manohar, Phys. Rev. D **59**, 074017 (1999).

[58] T. van Ritbergen, Phys. Lett. B **454**, 353 (1999).

[59] Y. Amhis *et al.* (Heavy Flavor Averaging Group), arXiv:1207.1158.

[60] G. C. Fox and S. Wolfram, Phys. Rev. Lett. **41**, 1581 (1978).

[61] See Supplemental Material at http://link.aps.org/supplemental/10.1103/PhysRevD.95.072001 for the differential branching fraction (GGOU) for semileptonic *B* decays as a function of the electron momentum (in the $\Upsilon(4S)$ rest frame).